

Shigella effector IpaH1.4 subverts host E3 ligase RNF213 to evade antibacterial immunity

Received: 17 October 2024

Accepted: 21 March 2025

Published online: 01 April 2025

Check for updates

Xindi Zhou ^{1,5}, Huijing Zhang ^{1,2,5}, Yaru Wang ^{1,3,5}, Danni Wang ^{4,5}, Zhiqiao Lin¹, Yuchao Zhang ¹, Yubin Tang¹, Jianping Liu ¹, Yu-Feng Yao ⁴ ✉, Yixiao Zhang ^{1,2} ✉ & Lifeng Pan ^{1,3} ✉

Ubiquitination plays vital roles in modulating pathogen-host cell interactions. RNF213, a E3 ligase, can catalyze the ubiquitination of lipopolysaccharide (LPS) and is crucial for antibacterial immunity in mammals. *Shigella flexneri*, an LPS-containing pathogenic bacterium, has developed mechanisms to evade host antibacterial defenses during infection. However, the precise strategies by which *S. flexneri* circumvents RNF213-mediated antibacterial immunity remain poorly understood. Here, through comprehensive biochemical, structural and cellular analyses, we reveal that the E3 effector IpaH1.4 of *S. flexneri* can directly target human RNF213 via a specific interaction between the IpaH1.4 LRR domain and the RING domain of RNF213, and mediate the ubiquitination and proteasomal degradation of RNF213 in cells. Furthermore, we determine the cryo-EM structure of human RNF213 and the crystal structure of the IpaH1.4 LRR/RNF213 RING complex, elucidating the molecular mechanism underlying the specific recognition of RNF213 by IpaH1.4. Finally, our cell based functional assays demonstrate that the targeting of host RNF213 by IpaH1.4 promotes *S. flexneri* proliferation within infected cells. In summary, our work uncovers an unprecedented strategy employed by *S. flexneri* to subvert the key host immune factor RNF213, thereby facilitating bacterial proliferation during invasion.

Ubiquitination is one of the most important and versatile post-translational modifications in mammals, which involves the covalent attachment of ubiquitin to a specific target substrate, a process mediated by a cascade of three different enzymes including an E1 activating enzyme, an E2 conjugating enzyme, and an E3 ligase^{1–4}. Notably, in addition to conventional protein substrates, non-proteinaceous substrates, such as lipopolysaccharide (LPS), relevant

sugars and nucleotides, are also found to be modified by ubiquitination^{5–7}. Ubiquitination plays essential roles in a multitude of cellular processes, such as proteasomal degradation, DNA repair, signal transduction, autophagy and immune responses^{2,3,8–10}. Particularly, in ubiquitination-mediated antimicrobial selective autophagy (also named as xenophagy)¹¹, the host immune system can utilize specific E3 ligases to mark intracellular invading pathogens with ubiquitin

¹State Key Laboratory of Chemical Biology, Shanghai Institute of Organic Chemistry, University of Chinese Academy of Sciences, Chinese Academy of Sciences, Shanghai 200032, China. ²Interdisciplinary Research Center on Biology and Chemistry, Shanghai Institute of Organic Chemistry, Chinese Academy of Sciences, Shanghai, China. ³School of Chemistry and Materials Science, Hangzhou Institute for Advanced Study, University of Chinese Academy of Sciences, 1 Sub-lane Xiangshan, Hangzhou 310024, China. ⁴Laboratory of Bacterial Pathogenesis, Shanghai Institute of Immunology, Shanghai Jiao Tong University School of Medicine, Shanghai, China. ⁵These authors contributed equally: Xindi Zhou, Huijing Zhang, Yaru Wang, Danni Wang.

✉ e-mail: yfiao@sjtu.edu.cn; y Zhang@mail.sioc.ac.cn; panlf@sioc.ac.cn

molecules, which are subsequently recognized by ubiquitin-binding autophagy receptors, such as Optineurin, p62, and NDP52^{12–17}, thereby guiding the pathogens for autophagic degradation to prevent infection spread^{18–20}. Moreover, ubiquitination is widely involved in activating innate immune pathways, such as the NF- κ B pathway, which promotes the expression of antimicrobial peptides and cytokines to restrict the proliferation of invading pathogens^{21–23}. This dual role of ubiquitination, both in tagging pathogens for autophagic degradation and promoting inflammatory responses, positions it as a key regulator in host immune defenses against a wide range of microbial invaders²⁴.

RNF213 is a giant multifunctional E3 ligase containing more than 5000 amino acids, and is the only known protein possessing both AAA + ATPase and E3 ligase activities in the human proteome^{25,26}. RNF213 was first identified as a susceptibility gene for Moyamoya disease (MMD), a rare cerebrovascular disorder characterized by progressive stenosis of the cerebral arteries^{27,28}. RNF213 has been demonstrated to influence angiogenesis and vascular remodeling, although its precise molecular function in vascular development is still under investigation^{26,29}. In addition, RNF213 is also reported to serve as a positive regulator of lipid droplets³⁰, which are cellular lipid storage organelles and play vital roles in the regulation of inflammation and immunity^{31,32}. Recently, RNF213 is implicated in the regulation of antimicrobial immunity, and has emerged as a key player to combat various invasive pathogens, including viruses, bacteria, parasites, and chlamydiae^{3,33–37}. Particularly, RNF213 can directly mediate the ubiquitination of bacterial LPS on the surface of *Salmonella Typhimurium*, and recruit the linear ubiquitin chain assembly complex (LUBAC), a key E3 ligase complex capable of catalyzing linear ubiquitination, to trigger downstream antimicrobial selective autophagy and cellular autonomic immunity for eliminating invading bacteria⁵. Given the critical roles of RNF213 in host antibacterial immunity, whether RNF213 might be targeted and hijacked by LPS-containing bacterial pathogens remains an open question.

S. flexneri is a type of LPS-containing gram-negative bacterial pathogen. It is the leading cause of shigellosis, and causes millions of infections with significant human fatalities worldwide each year^{38,39}. Interestingly, *S. flexneri* has evolved different strategies to evade ubiquitination-mediated host immune defenses during infection^{40–45}. Particularly, *S. flexneri* can secrete relevant IpaH family E3 effectors to exploit the host's ubiquitination system to promote the ubiquitination and subsequent degradation of key host proteins essential for ubiquitination-mediated antibacterial responses^{42,44,46}. IpaH family E3 effector of *S. flexneri* contains a conserved C-terminal catalytic E3 ligase (NEL) domain and a N-terminal substrate-binding leucine-rich repeat (LRR) domain that confers specificity for targeting different host substrates^{47,48}. For instance, IpaH9.8 can directly target NEMO, a key ubiquitin-binding adapter of the NF- κ B signaling pathway, thereby inhibiting pro-inflammatory cytokine production and diminishing the host's inflammatory response⁴². Moreover, two highly similar IpaH family E3 effectors, IpaH1.4 and IpaH2.5, were recently demonstrated to suppress NF- κ B activation and antimicrobial selective autophagy by targeting LUBAC^{44,49}. However, whether there are other host proteins critical for antibacterial immunity that could be targeted by *S. flexneri* IpaH1.4 is still largely unknown.

In this study, by using IpaH1.4 as a bait via an affinity purification coupled with mass spectrometric analysis, we firstly discover that IpaH1.4 can associate with human RNF213. Subsequently, we demonstrate that IpaH1.4 directly interacts with human RNF213, and mediates the ubiquitination and proteasomal degradation of RNF213 in cells. Further biochemical, cryogenic electron microscopy (cryo-EM) and X-ray crystallography analyses uncover that IpaH1.4 can specifically recognize the RING domain of RNF213 through its LRR domain. The determined cryo-EM structure of human RNF213 and the crystal structure of the IpaH1.4 LRR/RNF213 RING complex elucidate the molecular mechanism by which IpaH1.4 specifically target RNF213.

Finally, our relevant cell-based infection assays demonstrate that the targeting of RNF213 by IpaH1.4 facilitates the proliferation of *S. flexneri* in host cells. Taken together, our work uncovers that *S. flexneri* can adopt IpaH1.4 to directly target and subvert host RNF213, thereby escaping from RNF213-mediated host immune defenses to facilitate its proliferation in infected host cells. Our findings suggest that targeting the IpaH1.4/RNF213 interaction may offer therapeutic strategies for combating *S. flexneri* infections and modulating host immune responses.

Results

RNF213 is a host targeting protein of *S. flexneri* IpaH1.4

In order to investigate whether there are additional host proteins that might be targeted by IpaH1.4 during the invasion of *S. flexneri*, we performed a biochemical affinity purification coupled with mass spectrometric (MS) analysis-based assay to identify IpaH1.4-binding proteins in HEK293F cells (Fig. 1a). The FLAG-tagged catalytically inactive IpaH1.4 C368A mutant and the substrate-binding LRR domain of IpaH1.4 were individually overexpressed in HEK293F cells, and then were enriched and pulled down via anti-FLAG beads. Subsequently, the related human proteins that can associate with the two IpaH1.4 proteins were detected by mass spectrometric-based analysis. In addition to the previously known IpaH1.4-binding proteins HOIP and HOIL-1L^{44,49}, one of the identified strongest candidates for potentially binding to IpaH1.4 was the giant human E3 ligase RNF213 (Fig. 1b and Supplementary Fig. 1), which was recently demonstrated to function as a key player in antibacterial immunity^{5,26}. To critically test the potential interaction between IpaH1.4 and RNF213, we firstly performed relevant GST pull-down assays, which showed that the GST-tagged IpaH1.4 but not the GST tag can interact with the full-length RNF213 (Fig. 1c). Further co-immunoprecipitation (Co-IP) assays confirmed that the full-length RNF213 as well as the RNF213(371–5207) fragment that lacks the N-terminal intrinsically disordered region of RNF213 based on previous reports^{50,51}, and our sequence analyses (Supplementary Fig. 2a, b), can well interact with IpaH1.4 in co-transfected HEK293T cells (Fig. 1d). To further critically test the direct interaction between RNF213 and IpaH1.4, we sought to purify full-length RNF213 proteins to conduct relevant biochemical assays. However, the purified full-length RNF213 proteins from HEK293F cells tend to form large aggregates and display poor homogeneity (Supplementary Fig. 3a, b), preventing further detailed biochemical and structural characterizations. Fortunately, the purified RNF213(371–5207) fragment, which can still well interact with intracellular IpaH1.4 (Fig. 1d), is a homogeneous monomer in solution based on our multi-angle light scattering (MALS) analysis (Supplementary Fig. 3c). As expected, using size exclusion chromatography (SEC)-based assays with purified RNF213(371–5207) and the full-length IpaH1.4 proteins, we demonstrated that IpaH1.4 can directly interact with RNF213 (Fig. 1e, f).

The proteasomal degradation of RNF213 mediated by IpaH1.4

Given that the IpaH family members can induce the degradation of their targeting substrates via the ubiquitin-proteasome system (UPS), we wondered whether IpaH1.4 could mediate the ubiquitination and proteasome dependent degradation of RNF213. Following a well established method used in previous studies^{44,49}, we utilized UBA1 as the E1 enzyme and UBE2D1 as the E2 enzyme to set up an in vitro ubiquitination assay of IpaH1.4 with its potential substrate RNF213. Using this in vitro ubiquitination assay together with the purified catalytically inactive C4516A mutant of RNF213(371–5207), which loses the E3 enzymatic activity of its RZF domain and cannot undergo auto-ubiquitination⁵⁰, we revealed that IpaH1.4 can directly catalyze the ubiquitination of RNF213 in vitro (Fig. 2a, b). Remarkably, the ubiquitination of RNF213 catalyzed by IpaH1.4 requires the presence of ATP, UBA1 (E1), UBE2D1 (E2), and IpaH1.4 (E3) (Fig. 2a). Removal of ATP or any of the three enzymes results in the failure of the formation of the ubiquitinated RNF213 (Fig. 2a), confirming that the ubiquitination of

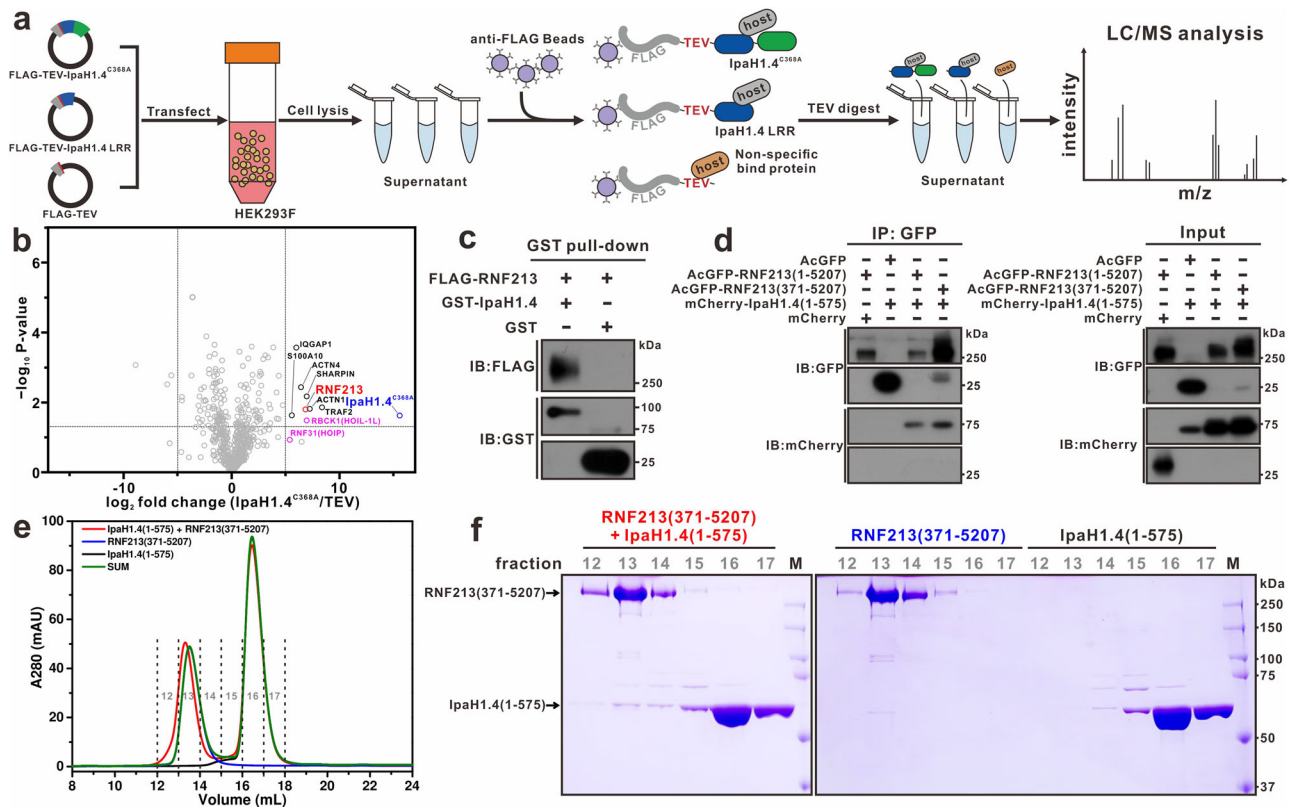


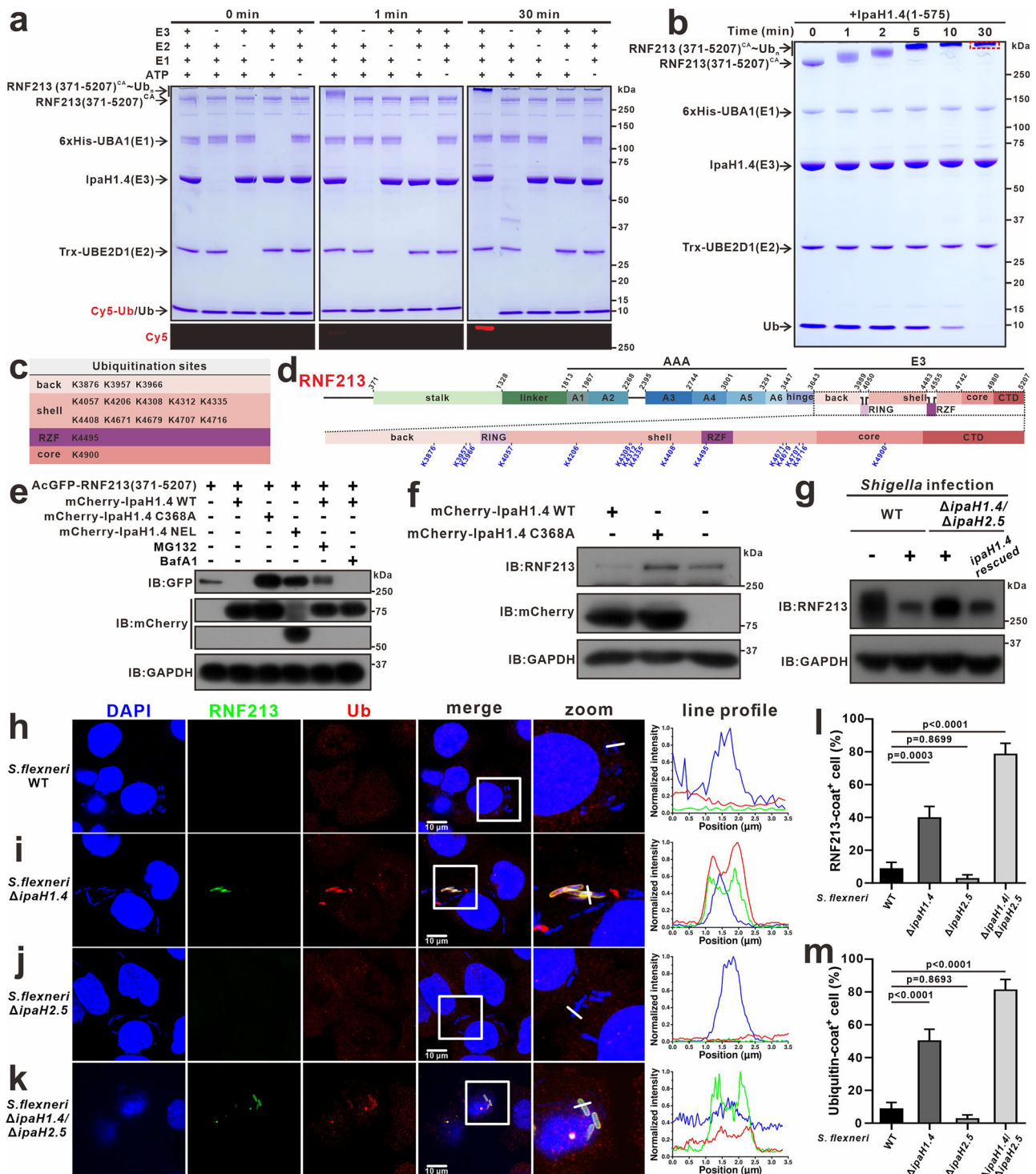
Fig. 1 | The *S. flexneri* effector IpaH1.4 can directly interact with RNF213. **a** A schematic diagram showing the strategy used for the identification of IpaH1.4-binding proteins in HEK293F cells based on a biochemical affinity purification coupled with mass spectrometric analyses. **b** The volcano plot illustrating the comparison of FLAG pull-downs from HEK293F cell lysates ($n = 3$) overexpressing the FLAG-TEV-IpaH1.4 C368A mutant with the empty plasmid vector FLAG-TEV serving as the control in the affinity purification coupled to mass spectrometry (AP-MS) analyses. Notably, a two-tailed unpaired Student's t test analysis was performed for the analysis of this AP-MS data. Proteins significantly enriched in the anti-FLAG bead pull-downs are annotated for clarity (p value < 0.05 , fold change > 32 ; except for HOIP). The identified RNF213 is highlighted in red, HOIP and HOIL-1L are highlighted in purple, and IpaH1.4 is highlighted in blue. **c** GST pull-down assays of the GST-tagged IpaH1.4 or the GST tag with the FLAG-tagged full-length human RNF213 expressed in HEK293F cells. This experiment was independently repeated twice.

d Co-immunoprecipitation assays showing the mCherry-tagged full-length IpaH1.4 can interact with the AcGFP-tagged human full-length RNF213 and the RNF213(371-5207) fragment in HEK293T cells. IP immunoprecipitation, IB immunoblotting. This experiment was independently repeated twice. **e** Size exclusion chromatography (SEC)-based analysis of the interaction between RNF213(371-5207) and IpaH1.4(1-575) performed on the Superose 6 increase 10/300 GL column. In this panel, "SUM" stands for the theoretical sum of RNF213(371-5207) and IpaH1.4(1-575) profiles, and A280 stands for the absorbance at 280 nm. For the reconstitution of the binding between RNF213(371-5207) and IpaH1.4(1-575), the RNF213 and IpaH1.4 proteins were expressed and purified separately, and then mixed together prior to the (SEC)-based analysis. **f** SDS-PAGE combined with Coomassie blue staining analyses showing the protein components of the corresponding fraction 12 to 17 collected from the SEC-based experiments in (e).

RNF213 by IpaH1.4 occurs through a canonical ubiquitination mechanism. Further mass spectrometry-based analysis of the ubiquitinated RNF213 band from the *in vitro* ubiquitination assay mediated by IpaH1.4 (Fig. 2b), revealed that there are multiple ubiquitin modification sites on RNF213(371-5207) catalyzed by IpaH1.4 (Fig. 2c and Supplementary Fig. 3d), all of which are located in the E3 module of RNF213 (Fig. 2d). Notably, *S. flexneri* contains two strikingly similar IpaH family effectors IpaH1.4 and IpaH2.5^{44,49}, which have only two residues different in their substrate-binding LRR domains (Supplementary Fig. 4a). Not surprisingly, based on our *in vitro* ubiquitination assays, RNF213 can be effectively ubiquitinated by IpaH2.5 (Supplementary Fig. 4b), suggesting that both IpaH1.4 and IpaH2.5 can directly target host RNF213. Despite the E3 activity of RNF213 contributing to the host immune response during pathogenic infections⁵, the purified RNF213(371-5207) was incapable to ubiquitinate IpaH1.4 conversely *in vitro* (Supplementary Fig. 5a, b). To further elucidate the type of ubiquitin modification on RNF213 catalyzed by IpaH1.4, we constructed 9 different ubiquitin mutants, which contain additional N-terminal extension sequences and/or specific mutations by replacing relevant lysine residues of ubiquitin with arginine residues (Supplementary Fig. 5c). Further *in vitro* ubiquitination assays revealed that

IpaH1.4 mainly catalyzes the K48-linked ubiquitination of RNF213 *in vitro* (Supplementary Fig. 5d), similar to other IpaH family proteins⁴⁷. Consistent with our biochemical results and the established role of K48-linked polyubiquitin as a proteasomal degradation signal, we observed that the co-expression of *Aequorea coerulescens* GFP-tagged (AcGFP) RNF213(371-5207) with the wild-type IpaH1.4 in HeLa cells led to a significant reduction in the cellular protein level of RNF213(371-5207) (Fig. 2e). Notably, this reduction of the RNF213(371-5207) protein level was abolished, when either the catalytically inactive IpaH1.4 C368A mutant or the isolated NEL domain of IpaH1.4 was co-expressed with RNF213(371-5207), or when cells were treated with the proteasomal inhibitor MG132 (Fig. 2e). These results well demonstrated that IpaH1.4 can mediate the cellular proteasomal degradation of RNF213 through its E3 activity. Consistently, expression of the wild type IpaH1.4 rather than the E3-dead C368A mutant of IpaH1.4 in HeLa cells can induce the degradation of endogenous RNF213 (Fig. 2f).

To further investigate whether RNF213 is a physiological substrate of IpaH1.4/2.5 during *S. flexneri* invasion, we firstly generated an RNF213-knockout HeLa cell line using CRISPR-Cas9 technology (Supplementary Fig. 6a, b). Then, RNF213-knockout HeLa cells were transfected with relevant passer transposon system to generate a stable cell



line expressing AcGFP-tagged wild-type RNF213 (Supplementary Fig. 6c, d). Subsequently, we infected the AcGFP-RNF213 stable HeLa cells with the wild-type *S. flexneri* M90T strain, the *ipaH1.4* knock-out (Δ *ipaH1.4*) *S. flexneri* strain, the *ipaH2.5* knock-out (Δ *ipaH2.5*) *S. flexneri* strain or the *ipaH1.4/ipaH2.5* double knock-out (Δ *ipaH1.4/ΔipaH2.5*) *S. flexneri* strain generated in our previous study⁴⁹. As expected, intracellular AcGFP-RNF213 signals can be well detected in cells infected with the Δ *ipaH1.4* *S. flexneri* strain or the Δ *ipaH1.4/ΔipaH2.5* *S. flexneri* strain, especially on the surface of invaded bacteria, while they are barely detectable in cells infected with the wild-type *S. flexneri* or the Δ *ipaH2.5* *S. flexneri* (Fig. 2h–l). Consistently, obvious ubiquitin-coat on the surface of invading bacteria can be observed in cells infected with

the *S. flexneri* Δ *ipaH1.4* strain or Δ *ipaH1.4/ΔipaH2.5* strain but not the wild-type *S. flexneri* or the Δ *ipaH2.5* *S. flexneri* strain (Fig. 2h–k, m). Consistent with our cellular data, infection of HeLa cells with the wild-type *S. flexneri* strain or the Δ *ipaH1.4/ΔipaH2.5* *S. flexneri* strain rescued with *ipaH1.4* but not the Δ *ipaH1.4/ΔipaH2.5* strain significantly induced the degradation of endogenous RNF213 in host cells (Fig. 2g). Given that RNF213 can directly mediate the ubiquitination of LPS on the surface of invading *Salmonella*⁵, these findings suggest that *S. flexneri* primarily employs its effector IpaH1.4 to degrade host RNF213 during invasion, thereby helping *S. flexneri* to escape from being marked by ubiquitination as well as related downstream antibacterial immune processes.

Fig. 2 | IpaH1.4 can mediate the ubiquitination and proteasomal degradation of RNF213. **a** In vitro ubiquitination assays of IpaH1.4 with the RNF213(371-5207) C4516A mutant using a mixture of the un-labeled ubiquitin (Ub) and the fluorescent Cy5-labeled ubiquitin (Cy5-Ub) in the presence E1 (UBA1), E2 (UBE2D1), E3 (IpaH1.4), and ATP or in the absence of E1 (UBA1), E2 (UBE2D1), E3 (IpaH1.4), or ATP. The below panels showing the red fluorescent Cy5-labeled ubiquitin signals near the gel loading wells, which are corresponding to the ubiquitinated RNF213 proteins. **b** In vitro ubiquitination assays of IpaH1.4 with the RNF213(371-5207) C4516A mutant using un-labeled ubiquitin (Ub). Notably, the ubiquitinated RNF213 band used for MS-based analysis to identify ubiquitination sites is indicated with a red dashed box. **c** The summary of the IpaH1.4-mediated ubiquitination sites of RNF213 identified by mass spectrometry-based analysis. **d** The distribution of the identified ubiquitination sites in **c** on the domain schemes of human RNF213. The domain boundaries and the potential ubiquitination sites are labeled with black and blue, respectively. **e** Immunoblot analyses of lysates from HeLa cells expressing AcGFP-tagged RNF213 without or with the mCherry-tagged wild type IpaH1.4, IpaH1.4 C368A mutant, or IpaH1.4 NEL domain in the absence or in the presence of proteasomal inhibitor MG132 or autophagy inhibitor bafilomycin A1 (BafA1). For MG132 or BafA1 treated cells, a final concentration of 20 μ M for MG132 or 100 nM for BafA1 were added into the culture medium 12 h before cell harvest. **f** Immunoblot

analyses of lysates from HeLa cells over-expressing the mCherry-tagged wild type IpaH1.4 or IpaH1.4 C368A mutant. The endogenous RNF213 protein levels were monitored by a specific RNF213 antibody. **g** Immunoblot analyses of the cell lysates from HeLa cells infected for 24 h with the wild type (WT) *S. flexneri* strain, the *ipaH1.4/ipaH2.5* double knock-out (Δ *ipaH1.4/ΔipaH2.5*) *S. flexneri* strain, or the Δ *ipaH1.4/ΔipaH2.5* *S. flexneri* strain rescued with *ipaH1.4*, respectively. The endogenous RNF213 protein levels were monitored by a specific RNF213 antibody. Representative confocal micrographs of RNF213-knockout HeLa cells stably expressing AcGFP-tagged wild type RNF213 at 4 h after infection with the wild type *S. flexneri* M90T strain (**h**), the *ipaH1.4* knockout (Δ *ipaH1.4*) *S. flexneri* (**i**), the *ipaH2.5* knockout (Δ *ipaH2.5*) *S. flexneri* (**j**) or the *ipaH1.4/ipaH2.5* double-knockout (Δ *ipaH1.4/ΔipaH2.5*) *S. flexneri* (**k**). HeLa cells were stained with a specific antibody to ubiquitin (red), and DAPI (blue) to show the invaded bacteria and the nuclei of cells. WT wild type; Scale bars, 10 μ m. Statistical result related to the percentage of cells containing cytosolic *S. flexneri* with RNF213-coat (**l**), or ubiquitin-coat (**m**) decorated on the surface at 4 h after infection. The data represent the mean \pm SEM of 47, 48, 40, and 37 cells for each group, presented in the same order as in (**l**) or in (**m**). An unpaired ordinary one-way ANOVA analysis followed by Sidak multiple comparisons test was used to define a statistically significant difference.

The cryo-EM structure of human RNF213

To elucidate the molecular basis underlying the specific recognition of RNF213 by IpaH1.4, we firstly purified the RNF213(371-5207)/IpaH1.4 complex by mixing excess amounts of IpaH1.4 with human RNF213(371-5207) followed by SEC-based separation (Supplementary Fig. 7a, b). The purified RNF213(371-5207)/IpaH1.4 complex exhibited reasonable homogeneity based on our negative staining electron microscopy analysis (Supplementary Fig. 7c). Subsequently, using the cryo-EM method, we obtained the final consensus density map of the RNF213(371-5207)/IpaH1.4 complex to an overall resolution of 3.46 Å (Supplementary Fig. 8a–c and Supplementary Table 1). Unfortunately, based on the solved cryo-EM density map, we could only build a high-confidence model of RNF213, which mainly contains five structural segments, the N-terminal stalk, the middle six AAA units-containing AAA ring, the C-terminal multi-domain E3 module, and the stalk/AAA ring-connecting linker as well as the AAA ring/E3 module-connecting hinge (Fig. 3a–c). Similar to previously determined cryo-EM structure of mouse RNF213⁵⁰, human RNF213 folds into a compact zig-zag conformation from its N-terminal stalk to the C-terminal CTD (Fig. 3a–c). Notably, the E3 module of human RNF213 is composed of six sub-domains, namely back, RING, shell, RZF, core and CTD, and has direct contacts with the stalk and AAA ring modules through its back and CTD, respectively (Fig. 3a–c). The RING domain swinging between the E3 back and E3 shell was previously thought to be the only domain with E3 enzymatic activity just like other RING-type E3 ligases^{52,53}, however recent studies well demonstrated that RNF213 can also perform its E3 ligase function in a RING-independent manner⁵. Particularly, RNF213 can directly ubiquitylate LPS on the surface of invading *Salmonella* through its active C4516 residue within the RZF domain⁵. Notably, the electron densities of the RING and RZF regions are relatively weak, likely owing to their conformational flexibilities (Fig. 3b). Further detailed structural analyses revealed that, among the six AAA units of RNF213, only AAA3 and AAA4 harbor all the essential catalytic residues and functional motifs for exerting ATP-binding and ATP-hydrolysis (Supplementary Fig. 9), while the AAA1, AAA5, and AAA6 are completely inactive due to the lack of relevant key structural elements (Supplementary Fig. 9a, e, f). Intriguingly, in the cryo-EM structure of human RNF213, the AAA2 of RNF213 contains a well defined ATP molecule, but lacks the catalytic arginine finger for ATP hydrolysis (Fig. 3b, c and Supplementary Fig. 9b), suggesting that it is catalytically incompetent, in line with a previous study⁵⁰. Moreover, there is a distinct insertion existed between the AAA2 and AAA3 of RNF213 (Fig. 3a–c). Further structural comparison analyses showed that the overall structure of human RNF213 is very similar to that of previously

determined the apo-form mouse RNF213⁵⁰, however the relative orientation and gap between the N-terminal segment of stalk and the E3 module of human RNF213 is very different from that of mouse RNF213 (Supplementary Fig. 10a–f). In addition, the density map of the RZF domain within the E3 module of human RNF213 is much better than that of mouse RNF213 (Supplementary Fig. 10g–i).

IpaH1.4 recognizes RNF213 RING domain through its LRR domain

After fitting the whole RNF213 structure model into the cryo-EM density map, we found an extra weak density around the RING domain of RNF213, which does not belong to RNF213 but can be partially matched with the IpaH1.4 LRR domain (Supplementary Fig. 11). Further local refinement focusing around the RNF213 E3 module resulted in a local density map with a much-improved resolution for fitting the IpaH1.4 LRR domain (Fig. 3d, e and Supplementary Fig. 8). Based on the refined local density map, IpaH1.4 LRR can directly bind to the RING domain of RNF213 through its concave side (Fig. 3d, e). However, due to the low resolution of the local density map, we were unable to observe the detailed interactions between interface residues of RNF213 RING and IpaH1.4 LRR. Moreover, we also could not identify any density belonging to the IpaH1.4 NEL domain, likely due to its dynamic nature for facilitating its ubiquitination on multiple sites of RNF213. Importantly, consistent with our structural data, when mapping aforementioned MS-identified ubiquitination sites of RNF213 onto the cryo-EM structure of RNF213, we found that they are all adjacent to RNF213 RING and are reachable for the IpaH1.4 NEL domain (Fig. 2c, d and Supplementary Fig. 12a–c).

Using SEC-based biochemical assays, we further confirmed that the isolated RNF213 RING (residues 3990-4056) can directly interact with the IpaH1.4 LRR domain (residues 38-273) (Fig. 4a). In addition, quantitative isothermal titration calorimetry (ITC) analysis uncovered that IpaH1.4 LRR binds to RNF213 RING with a dissociation constant (K_D) value of \sim 0.18 μ M (Fig. 4b). Consistent with our cryo-EM data, further analytical ultracentrifugation-based assay revealed that RNF213 RING and IpaH1.4 LRR can associate with each other to form a stable 1:1 stoichiometric complex in solution (Fig. 4c).

Crystal structure of the RNF213 RING/IpaH1.4 LRR complex

In order to elucidate the detailed binding mode between RNF213 RING and IpaH1.4 LRR, we solved the complex structure of RNF213 RING and IpaH1.4 LRR to 1.70 Å resolution using X-ray crystallographic method (Supplementary Table 2). As expected, in the RNF213 RING/IpaH1.4 LRR complex structure, IpaH1.4 LRR forms a horseshoe-shape fold, and

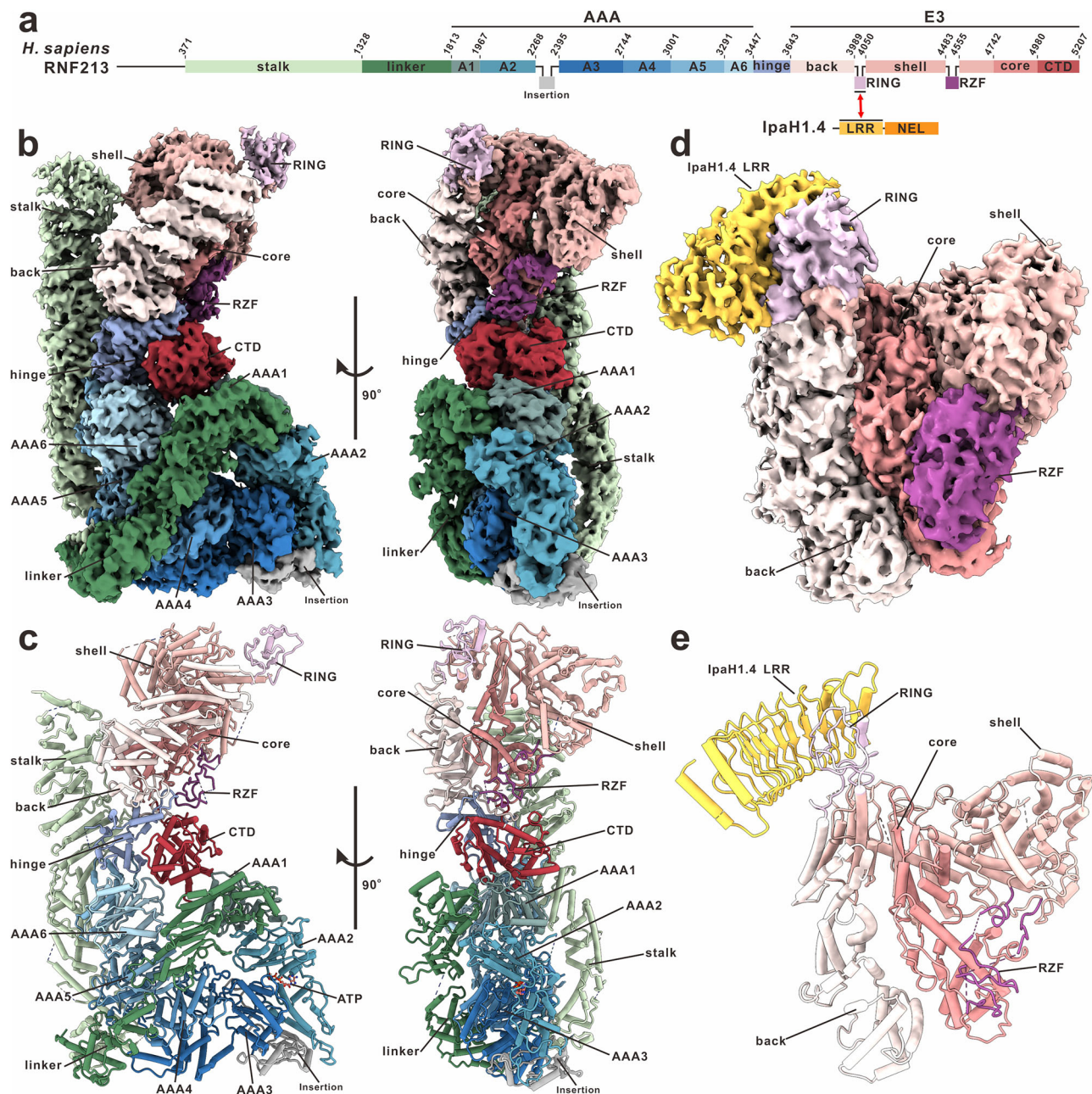
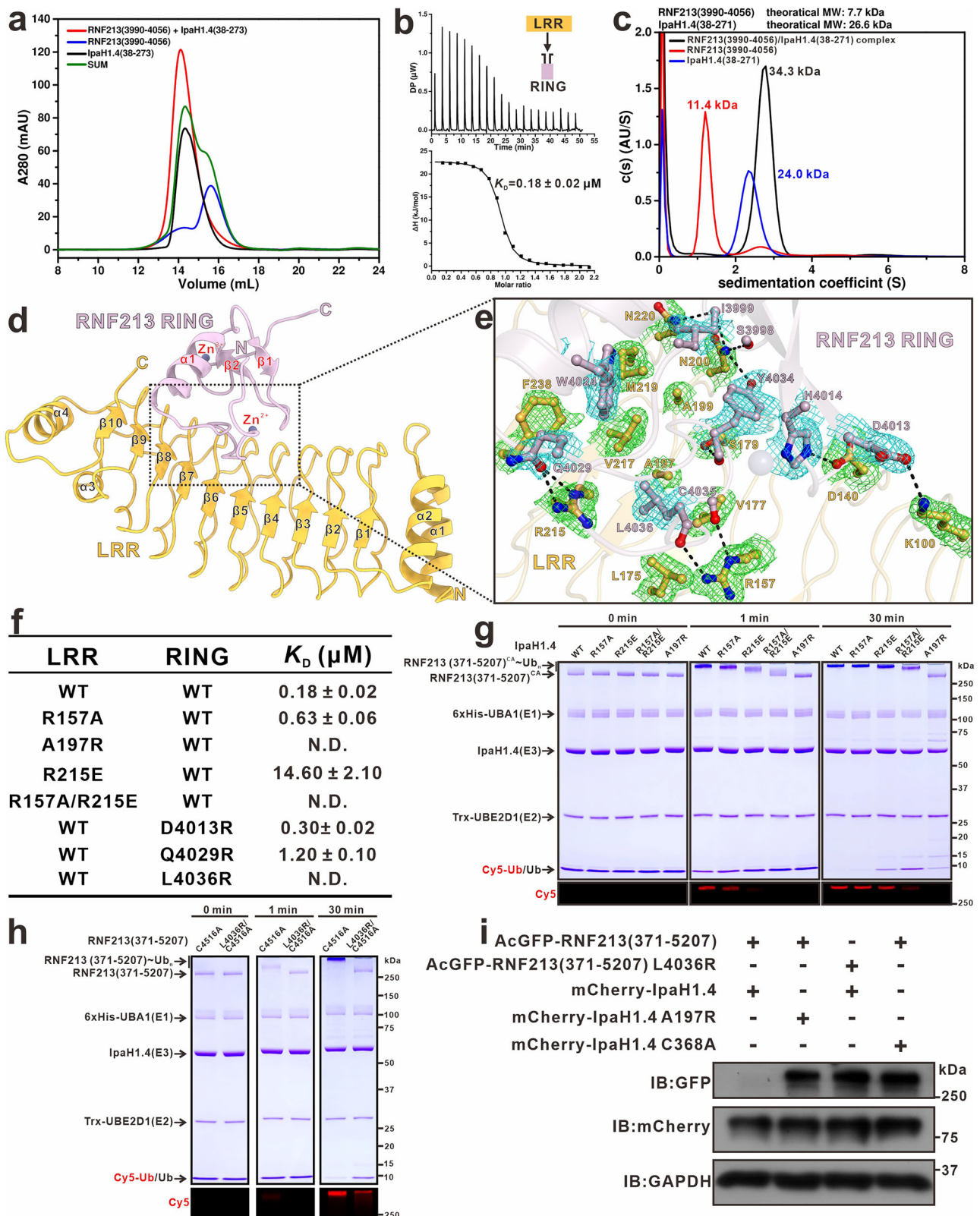


Fig. 3 | The cryo-EM structure of human RNF213 with IpaH1.4. **a** A schematic diagram showing the domain organizations of human RNF213 and *S. flexneri* IpaH1.4. In this drawing, the interaction between these two proteins is indicated by a two-way red arrow, and the domain boundaries of RNF213 are further labeled. The color scheme for domains of RNF213 and IpaH1.4 presented in this panel is used throughout all figures. **b** The front and side views of the cryo-EM map of human

RNF213. **c** The front and side views of the cryo-EM structure of human RNF213 with the same orientation and color scheme as in **(b)**. **d** The local refined cryo-EM map of the E3 module region of RNF213 with clear additional density (yellow) around the RING domain of RNF213, which is partially matched with the IpaH1.4 LRR domain. **e** The fitted structure model of RNF213 E3 module in complex with IpaH1.4 LRR based on the local refined cryo-EM map in **(d)**.

directly binds to RNF213 RING through its concave side (Fig. 4d). No significant structural changes can be observed in the IpaH1.4 LRR domain upon its binding to RNF213 RING (Supplementary Fig. 13a). Concurrently, in the complex structure, RNF213 RING that mainly consists of one N-terminal α -helix followed by two short C-terminal anti-parallel β -strands, adopts a unique architecture containing two Zn^{2+} ions to engage with the $\beta 2$ and $\beta 4$ to $\beta 9$ leucine-rich repeat region of IpaH1.4 LRR, burying a total surface area of $\sim 693 \text{ \AA}^2$ (Fig. 4d). Further structural comparison analysis revealed that the overall structure of human RNF213 RING in the RNF213 RING/IpaH1.4 LRR complex is similar to that of the *apo*-form mouse RNF213 RING (Supplementary Fig. 13b).

Detailed structural analysis of the RNF213 RING/IpaH1.4 LRR complex unraveled that the specific interaction between IpaH1.4 LRR and RNF213 RING is mediated by both hydrophobic contacts and polar interactions (Fig. 4e and Supplementary Fig. 14a, b). Specifically, the hydrophobic side chains of I3999, W4024 and L4036 of RNF213 RING form hydrophobic contacts with the hydrophobic side chains of L175, V177, A197, A199, V217, M219, and F238 as well as the aliphatic side chain groups of R215 from IpaH1.4 LRR (Fig. 4e and Supplementary Fig. 14a). In parallel, the positively charged side chain of K100 in IpaH1.4 LRR forms a salt bridge with the negatively charged side chain of D4013 from RNF213 RING (Fig. 4e and Supplementary Fig. 14b).



Concurrently, the side chains of D140, N200 and R215 in IpaH1.4 LRR form three hydrogen bonds with the side chains of H4014, Y4034 and Q4029 in RNF213 RING (Fig. 4e). In addition, the side chains of R157, S179, N200, and N220 residues of IpaH1.4 LRR couple with the backbone carboxyl groups of S3998, I3999, Y4034, C4035, and L4036 from RNF213 RING to form six specific hydrogen bonds (Fig. 4e). Using site-directed mutagenesis-based biochemical assays, we further validated

the specific interactions between RNF213 RING and IpaH1.4 LRR found in the complex structure. In keeping with our structural data, mutations of key binding interface residues either from IpaH1.4 LRR or RNF213 RING, such as the R157A, A197R, R215E and R157A/R215E mutations of IpaH1.4 LRR or the D4013R, Q4029R and L4036R mutations of RNF213 RING, all significantly reduced or essentially abolished the interaction of RNF213 RING with IpaH1.4 LRR in our ITC-based

Fig. 4 | IpaH1.4 binds to RNF213 RING through its LRR domain. **a** Size exclusion chromatography-based analysis of the interaction between RNF213(3990-4056) and IpaH1.4(38-273) performed on the Superdex 75 10/300 GL column. In this panel, “SUM” stands for the theoretical sum of RNF213(3990-4056) and IpaH1.4(38-273) profiles, and A280 stands for the absorbance at 280 nm. **b** ITC-based measurement of the binding affinity of RNF213(3990-4056) with IpaH1.4(38-273). The dissociation constant (K_D) error is the fitted error obtained from the data analysis software when using the one-site binding model to fit the ITC data. DP the differential power measured by the ITC machine, ΔH the heat change measured by the ITC machine. **c** The sedimentation velocity data of the purified RNF213(3990-4056), IpaH1.4(38-271) and the RNF213(3990-4056)/IpaH1.4(38-271) complex showing that RNF213 RING can interact with IpaH1.4 LRR to form a stable 1:1 stoichiometric complex in solution. **c**(s) continuous sedimentation coefficient distribution, MW molecular weight. **d** Ribbon diagram showing the overall structure of the RNF213 RING/IpaH1.4 LRR complex. In this drawing, the two coordinated Zn^{2+} ions of RNF213 RING are further indicated in the ball model. **e** The ribbon-stick-ball model showing the detailed binding interface between RNF213 RING and IpaH1.4 LRR in the complex structure. In this drawing, the relevant side chains as well as backbone groups of the key interface residues are shown in the stick-ball mode, and the

related hydrogen bonds and salt bridges involved in the RNF213 RING/IpaH1.4 LRR interaction are shown as dotted lines. The 2mFo-DFc map of the side chains of key interface residues in the structure of the RNF213 RING/IpaH1.4 LRR complex showing that the electron densities can be clearly assigned. The electron density map is shown in mesh and colored by cyan (RNF213 RING) and green (IpaH1.4 LRR), respectively. **f** Summary of the ITC-measured binding affinities between different RNF213 RING and IpaH1.4 LRR variants. “N.D.” stands for the K_D value is not detectable; WT wild type. **g** In vitro ubiquitination assays of different IpaH1.4 variants with the RNF213(371-5207) C4516A mutant using a mixture of the un-labeled ubiquitin (Ub) and the fluorescent Cy5-labeled ubiquitin (Cy5-Ub). The below panels showing the red fluorescent Cy5-labeled ubiquitin signals near the gel loading wells, which are corresponding to the ubiquitinated RNF213 proteins. This experiment was independently repeated twice. **h** In vitro ubiquitination assays of IpaH1.4 with different RNF213(371-5207) variants using a mixture of the un-labeled ubiquitin (Ub) and the fluorescent Cy5-labeled ubiquitin (Cy5-Ub). This experiment was independently repeated twice. **i** Immunoblot analyses of cell lysates from HeLa cells co-expressing different AcGFP-tagged RNF213 and mCherry-tagged IpaH1.4 variants. This experiment was independently repeated twice.

assays (Fig. 4f and Supplementary Fig. 15a–g). In agreement with our aforementioned biochemical and structural results, further in vitro ubiquitination assays proved that mutations of key interface residues of IpaH1.4 or RNF213, such as the A197R mutation of IpaH1.4 or the L4036R mutation of RNF213 C4516A, largely attenuate or completely disrupt the ubiquitination of RNF213 imposed by IpaH1.4 (Fig. 4g, h). Concomitantly, the A197R mutation of IpaH1.4 or the L4036R mutation of RNF213(371-5207) can effectively dampen the IpaH1.4-induced degradation of cellular AcGFP-RNF213(371-5207) in co-transfected HeLa cells (Fig. 4i). Notably, the key interface residues of IpaH1.4 LRR for recognizing RNF213 can be also found in IpaH2.5 but are absent in other *S. flexneri* IpaH family proteins or *S. typhimurium* effector SspH1 and SspH2 (Supplementary Fig. 16a). Thus, IpaH1.4 and IpaH2.5 are likely the only two members in the IpaH family that can specifically target RNF213. Intriguingly, although the overall binding mode of IpaH1.4 LRR with RNF213 RING resembles that of the IpaH1.4 LRR/HOIP RING1 and IpaH1.4 LRR/HOIL-1L UBL interactions⁴⁹, the binding interface residues and buried surface areas of IpaH1.4 LRR for interacting with RNF213 RING, HOIP RING1, and HOIL-1L UBL are very different (Supplementary Fig. 16a–d).

The intracellular targeting analyses of RNF213 by IpaH1.4

To further validate whether IpaH1.4 can directly target RNF213 under physiological conditions, we also generated a specific cell line from RNF213-knockout HeLa cells with a stable expression of the RNF213 L4036R mutant, which is unable to interact with IpaH1.4 (Fig. 4f, h, i). Then, we over-expressed the mCherry-tagged E3-dead IpaH1.4 C368A mutant, the mCherry-tagged IpaH1.4 R157A/R215E/C368A and A197R/C368A mutants that can not bind to RNF213 RING, or the control mCherry tag in the AcGFP-RNF213 or AcGFP-RNF213 L4036R stable HeLa cell lines, which were further infected with *ipaH1.4/ipaH2.5* double-knockout ($\Delta ipaH1.4/\Delta ipaH2.5$) *S. flexneri* (Fig. 5a–e). As expected, the mCherry-tagged IpaH1.4 C368A but not the mCherry tag in the transfected AcGFP-RNF213 stable cells exhibited an obvious enrichment on the RNF213-coated bacteria in the cytoplasm (Fig. 5a, e, f), suggesting that RNF213 can effectively recruit IpaH1.4 to invaded *S. flexneri*. In contrast, the R157A/R215E/C368A and A197R/C368A mutants of IpaH1.4, both of which were demonstrated to lose their abilities to interact with RNF213 (Fig. 4f, g), are essentially unable to co-localize with the RNF213-coat decorated on the surface of invaded *S. flexneri* in the transfected AcGFP-RNF213 stable cells (Fig. 5b, c, f). Consistently, although the AcGFP-tagged RNF213 L4036R mutant can target the intracellular bacteria to form the RNF213-coat, it fails to recruit the E3-dead IpaH1.4 C368A mutant to the intracellular bacteria (Fig. 5d, f). Taken together, these data clearly demonstrated that the

specific RNF213 RING/IpaH1.4 LRR interaction is essential for the cellular targeting of IpaH1.4 to the RNF213-coat decorated on the surface of the intracellular invaded *S. flexneri*.

Targeting of RNF213 by IpaH1.4 promotes *Shigella* invasion

To further investigate the impact of the RNF213 RING/IpaH1.4 LRR interaction towards bacteria proliferation during *S. flexneri* invasion, we utilized the *ipaH1.4/ipaH2.5* double-knockout ($\Delta ipaH1.4/\Delta ipaH2.5$) *S. flexneri* strain and rescued it with the wild type *ipaH1.4* gene or relevant different *ipaH1.4* mutant gene (the R157A/R215E, A197R or C368A mutant of IpaH1.4). Then, we performed infection experiments in the wild type or RNF213-knockout HeLa cells using these *S. flexneri* strains. The results showed that the lack of RNF213 facilitates the invasion of the wild type *S. flexneri* but not *S. flexneri* $\Delta ipaH1.4/\Delta ipaH2.5$ (Supplementary Fig. 17a), suggesting that RNF213 can restrain the infection of *S. flexneri* and is likely one of the targets of IpaH1.4/2.5 in host cells. Notably, comparing with that of the wild type *S. flexneri*, the proliferation of *S. flexneri* $\Delta ipaH1.4/\Delta ipaH2.5$ strain in the wild type HeLa cells was largely attenuated (Fig. 5g). Meanwhile, the deficiency of RNF213 significantly facilitated the replication of the wild type *S. flexneri* in infected RNF213-knockout cells, compared with that of *S. flexneri* $\Delta ipaH1.4/\Delta ipaH2.5$ (Fig. 5g). These findings strongly suggested that *S. flexneri* relies on IpaH1.4/2.5 to target RNF213 thereby promoting its proliferation in infected host cells. Consistently, although *S. flexneri* $\Delta ipaH1.4/\Delta ipaH2.5$ strain rescued with the *ipaH1.4* R157A/R215E or A197R mutant has a similar infective activity towards the wild type HeLa cells as that of *S. flexneri* rescued with the wild type *ipaH1.4* (Supplementary Fig. 17b), the proliferation of *S. flexneri* rescued with *ipaH1.4* R157A/R215E, or A197R in infected cells was largely reduced compared with that of *S. flexneri* rescued with the wild type *ipaH1.4* (Fig. 5h), confirming that the targeting of RNF213 by IpaH1.4 is critical for promoting the proliferation of *S. flexneri* in host cells. Intriguingly, *S. flexneri* rescued with E3-dead *ipaH1.4* C368A shows a much lower infective activity than that of *S. flexneri* rescued with the wild type *ipaH1.4*, the *ipaH1.4* R157A/R215E mutant, or the *ipaH1.4* A197R mutant (Supplementary Fig. 17b), implying that the E3 activity of IpaH1.4 contributes to the infection of *S. flexneri* and there are other host targets of IpaH1.4 except for RNF213, in line with previous studies^{44,49,54}. Notably, our quantitative RT-PCR analyses revealed that the transcription levels of RNF213 in host cells are not significantly changed during the infection of *S. flexneri* (Supplementary Fig. 17c, d). Taken together, all these data well demonstrated that RNF213 can restrain *S. flexneri* proliferation in infected host cells, but *S. flexneri* can secrete E3 effector IpaH1.4/2.5 to specifically target and subvert RNF213, thereby facilitating its proliferation during invasion.

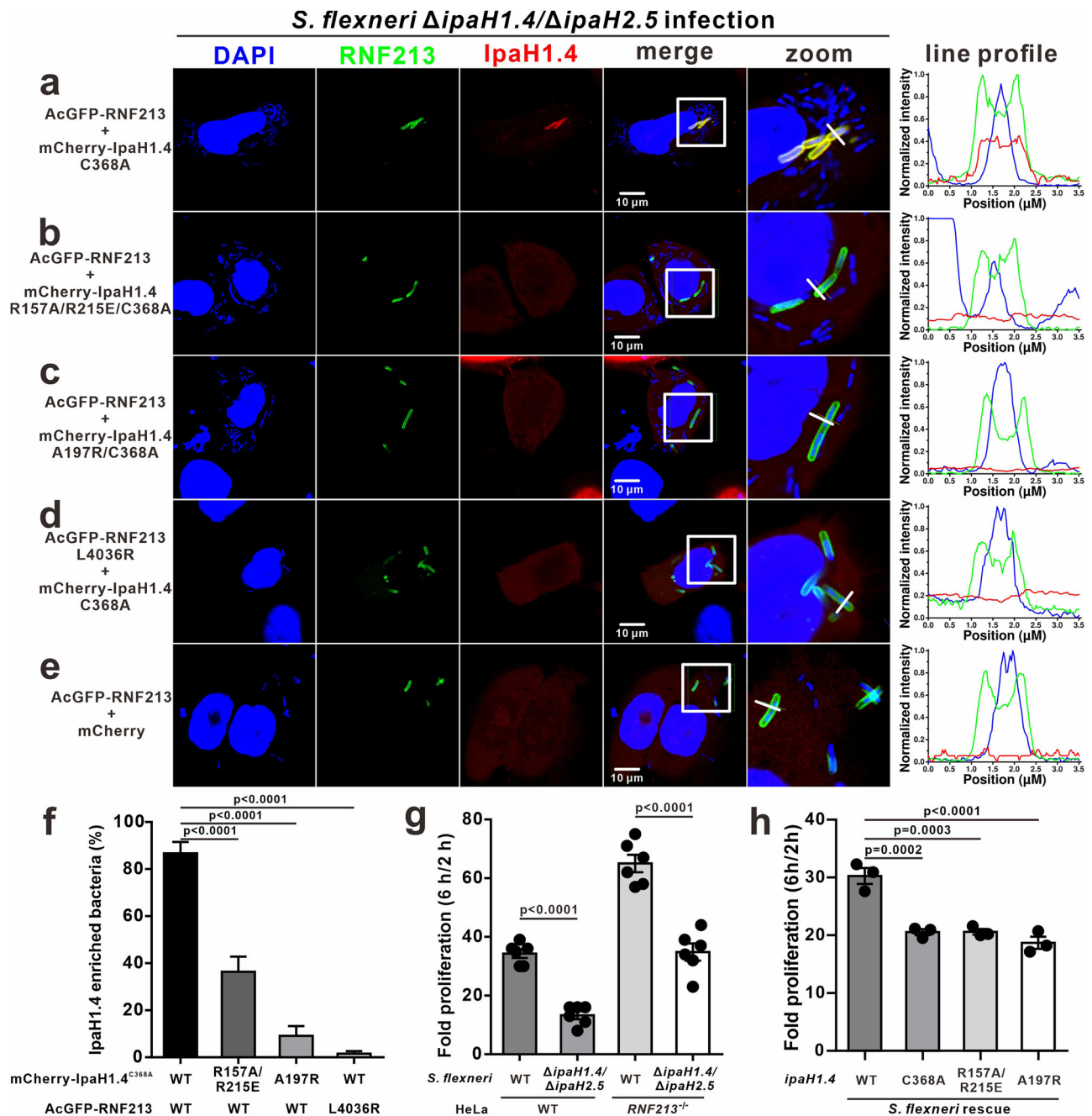


Fig. 5 | The cellular targeting of RNF213 by IpaH1.4 relies on the specific IpaH1.4 LRR/RNF213 RING interaction. **a–e** Representative confocal micrographs of *RNF213*-knockout HeLa cells stably expressing the AcGFP-tagged wild type *RNF213* or *RNF213* L4036R mutant were infected by the *ipaH1.4/ipaH2.5* double-knockout ($\Delta ipaH1.4/\Delta ipaH2.5$) *S. flexneri* strain 4 h after transfection of relevant different mCherry-tagged IpaH1.4 variant or the control mCherry tag and further expressed 24 h. HeLa cells were stained with the DAPI reagent for the nuclei. WT wild type; Scale bars, 10 μ m. **f** Statistical results related to the percentage of the IpaH1.4-positive *RNF213*-coats on cytosolic bacteria in (a–d). The data represent the mean \pm SEM of 40, 39, 41, and 43 cells for each group, presented in the same order as in (f). An unpaired ordinary one-way ANOVA analysis followed by Sidak multiple comparisons test was used to define a statistically significant difference. **g** Fold replication of the wild-type *S. flexneri* M90T and the *ipaH1.4/ipaH2.5* double-

knockout ($\Delta ipaH1.4/\Delta ipaH2.5$) *S. flexneri* in the infected wild type or *RNF213*-knockout HeLa cells calculated at 6 h time point normalized to 2 h time point after infection. Bacteria were counted by serial dilutions of cell lysate on LB agar plates. Data are presented as mean \pm SEM from three independent biological repeats. A two-tailed unpaired Student's *t* test analysis was used to define a statistically significant difference. **h** Fold replication of the *ipaH1.4/ipaH2.5* double-knockout ($\Delta ipaH1.4/\Delta ipaH2.5$) *S. flexneri* rescued with the wild type IpaH1.4 or different IpaH1.4 variant in infected wild type HeLa cells calculated at 6 h time point normalized to 2 h time point after infection. Bacteria were counted by serial dilution of cell lysate on LB agar plates. Data are presented as mean \pm SEM from three independent biological repeats. An unpaired ordinary one-way ANOVA analysis followed by Sidak multiple comparisons test was used to define a statistically significant difference.

Discussion

In this study, through comprehensive biochemical, structural and functional characterizations, we demonstrated that the *S. flexneri* effector IpaH1.4 can directly bind to the RING domain of the host

immune sensor RNF213 through its substrate-binding LRR domain, and induces the K48-linked ubiquitination as well as the proteasomal degradation of RNF213, thereby helping *S. flexneri* to escape from the RNF213-mediated ubiquitylation of LPS on its surface as well as the

downstream antimicrobial processes to facilitate its proliferation in host cells. It is worth mentioning that the targeting and subversion of host RNF213 by the *Shigella* effector IpaH1.4 is also uncovered in two recent reports from other groups^{55,56}. Importantly, based on the cryo-EM structure of RNF213 and the crystal structure of the RNF213 RING/IpaH1.4 LRR complex determined in this study, we elucidated the detailed binding mechanism of IpaH1.4 with RNF213, and obtained an intact structure model for the RNF213/IpaH1.4 LRR complex, in which IpaH1.4 LRR specifically recognizes RNF213 via binding to its RING domain (Supplementary Fig. 18). Thus, in addition to the two LUBAC subunits, HOIP and HOIL-1L^{44,49}, the key immune factor RNF213 of host cells can be also directly targeted and hijacked by IpaH1.4 during *S. flexneri* invasion. Notably, based on a previous report⁵, RNF213 works in the upstream of LUBAC during antibacterial immune processes. Interestingly, our structural comparison analysis revealed that the binding interfaces of IpaH1.4 LRR for interacting with RNF213 RING, HOIP RING1, and HOIL-1L UBL are different but highly overlapped (Supplementary Fig. 19), suggesting that RNF213, HOIP and HOIL-1L should be competitive in binding to IpaH1.4. Based on our ITC results in this study and a previous report⁴⁹, the binding affinity of IpaH1.4 LRR for HOIP RING1 (K_D - 1.0 μ M) or HOIL-1L UBL (K_D - 10.7 μ M) is much weaker than that for RNF213 RING (K_D - 0.18 μ M), therefore the upstream RNF213 rather than the downstream LUBAC was more likely to be firstly targeted by IpaH1.4 during *S. flexneri* invasion. Given the crucial roles of RNF213 in antimicrobial immunity, disrupting the IpaH1.4/RNF213 interaction represents a promising target for the future development of interventions aimed at augmenting host immunity against *S. flexneri* and related pathogens.

Previous studies well demonstrated that both RING domains of RNF213 and the RING-type E3 ligase RNF4 can specifically collaborate with the E2 enzyme UBE2N to conduct relevant K63-linked ubiquitination^{52,57}. Our structural alignment analysis of the RNF213 RING/IpaH1.4 LRR complex and the RNF4 RING/UBE2N-Ub/UBE2V1 complex (PDB ID: 5AIT [<https://doi.org/10.2210/pdb5AIT/pdb>]) revealed that IpaH1.4 LRR and UBE2N should be mutually exclusive in binding to the RING domain of RNF213, due to the potential steric exclusion (Supplementary Fig. 20). Therefore, in addition to triggering the K48-linked ubiquitination of RNF213 for proteasomal degradation, IpaH1.4 might also inhibit the E3 ligase activity of RNF213 RING by blocking its E2-binding. Notably, similar tactics were adopted by IpaH1.4 to hijack the host RBR-type E3 ligase HOIP⁴⁹. Interestingly, although the RNF213-mediated ubiquitylation of LPS on invaded bacteria is independent of the RING domain of RNF213⁵, many Moyamoya disease-associated mutations of RNF213 were found to locate in the RING domain, underscoring the critical role of RNF213 RING for human physiology⁵⁰. However, the precise function of the RNF213 RING domain remains to be elucidated in the future.

Intriguingly, our study together with previous reports showed that IpaH1.4 can directly target the host HOIP, HOIL-1L and RNF213 proteins, all of which are RING domain-containing E3 ligases^{44,49}. Thus, we wondered whether IpaH1.4 could generally bind to host RING domain-containing E3 ligases. To test this hypothesis, we chose the RING domain-containing E3 ligase MDM2, and conducted relevant GST pull-down assays. The result demonstrated that IpaH1.4 is unable to interact with MDM2 (Supplementary Fig. 21a). Indeed, further sequence alignment analysis revealed that the RING domain of MDM2 lacks the corresponding key residues of RNF213 RING for interacting with IpaH1.4 (Supplementary Fig. 21b). Therefore, IpaH1.4 is unable to generally target RING domain-containing E3 ligases. Interestingly, based on our proteomics data of the full length IpaH1.4 (Fig. 1b), the RING-type E3 ligase TRAF2 is another potential host target of IpaH1.4. Notably, TRAF2 was also identified as a potential binding target of IpaH2.5 in a previous study³⁴. Since TRAF2 is directly involved in the NF- κ B pathway, whether it could be directly targeted by IpaH1.4/2.5 is worthy of further investigation in the future.

Primates are the natural reservoirs of *S. flexneri*, while mice show million-fold higher doses of resisting *S. flexneri* infection⁵⁸. Interestingly, our sequence alignment analysis showed that all the key binding interface residues of RNF213 RING for interacting with IpaH1.4 LRR are highly conserved during evolution, including mouse (Supplementary Fig. 22a), suggested that mouse RNF213 should be also targeted by *S. flexneri* IpaH1.4. Using SEC and ITC-based analyses, we further confirmed the direct interaction between mouse RNF213 RING and IpaH1.4 LRR (Supplementary Fig. 22b, c). Therefore, the binding of IpaH1.4 to RNF213 RING is highly likely to be a general mechanism adopted by *S. flexneri* during invasion of different mammals. In the future, it will be interesting to know how mice can tolerate such high doses of *S. flexneri* infection.

Finally, based on our findings in this work and previous reports^{5,44,49}, we proposed a model depicting the targeting and subversion of host RNF213 by *S. flexneri* effector IpaH1.4/2.5 as well as the counteraction of *S. flexneri* with the relevant RNF213-mediated host antibacterial processes during invasion (Supplementary Fig. 23). In this model, once *S. flexneri* invades the cytosol of a host cell, its LPS molecules on the outer membrane will be specifically recognized by RNF213, which can further mediate the ubiquitylation of LPS and in turn recruit LUBAC to mediate the linear ubiquitination on the invading bacterial surface (Supplementary Fig. 23). Then, relevant downstream linear ubiquitin-binding proteins, such as NEMO and Optineurin, will be recruited to trigger inflammation and antibacterial selective autophagy processes to suppress replication of invading bacteria in the host cell (Supplementary Fig. 23). However, *S. flexneri* can secrete the E3 effector IpaH1.4/2.5 to directly target and hijack RNF213 via a specific interaction between IpaH1.4/2.5 LRR and RNF213 RING uncovered in this study (Supplementary Fig. 23). Subsequently, IpaH1.4/2.5 can mediate the K48-linked ubiquitination and proteasomal degradation of RNF213, thereby counteracting the relevant host antibacterial immune processes induced by RNF213 to facilitate the proliferation of *S. flexneri* in host cells (Supplementary Fig. 23).

Methods

Plasmids and mutagenesis

For recombinant protein expression in *E. coli*, the DNA fragments encoding desired proteins were cloned into a modified pRSFDuet-1 vector, which encodes a Trx-6 \times His (for expression of *S. flexneri* IpaH1.4 and IpaH2.5) or glutathione-S-transferase (GST) tag (for expression of RNF213 RING) followed by an HRV 3C protease cutting sequence before the multiple cloning sites. All the point mutations of constructs used in this study were introduced by standard PCR protocol. For expression in HeLa cells, the coding sequence for human RNF213 was inserted into a modified version of pAcGFP-C1 vector, resulting in a fusion protein with an N-terminal AcGFP tag. The coding sequence for IpaH1.4 was cloned into a modified version of pFLAG-CMV-1 vector, which has an N-terminal FLAG-mCherry tag. All mutations were introduced by standard PCR methods and verified by DNA sequencing. The cDNA of human RNF213 was purchased from the cDNA library of YouBio company (<http://www.youbio.cn/>, G111871). The full-length or truncated RNF213 were cloned into a modified pCAGGS vector for expression in HEK293F cells, which encodes a 3 \times FLAG-6 \times His-HRV 3C before the multiple cloning sites. The IpaH1.4 C368A mutant and IpaH1.4 NEL were cloned into a modified pCAGGS vector for expression in HEK293F cells, which encodes a 3 \times FLAG-TEV before the multiple cloning sites.

Protein expression and purification

For recombinant protein expressions in *E. coli*. Proteins were expressed in BL21 (DE3) *E. coli* cells induced by 100 μ M IPTG at 16 $^{\circ}$ C. For RNF213 RING proteins expression, additional 0.1 mM ZnCl₂ was added into the culture medium to improve protein folding before IPTG

induction. The bacterial cell pellets were lysed by the ultrahigh pressure homogenizer FB-110XNANO homogenizer machine (Shanghai Litu Machinery Equipment Engineering Co., Ltd.). Then, the lysate was spun down by centrifugation at $37,000 \times g$ for 30 min to remove the pellets fractions. Trx-6×His-tagged proteins were purified by Ni²⁺ Sepharose excel beads (GE Healthcare, 17371201) affinity chromatography in the binding buffer (50 mM Tris, 500 mM NaCl, and 5 mM imidazole at pH 7.9). GST fusion proteins were affinity purified by glutathione sepharose 4B beads (GE Healthcare, 17075601) with a column buffer containing 20 mM Tris, 100 mM NaCl, 1 mM dithiothreitol (DTT) at pH 7.5. Each recombinant protein was further purified by size-exclusion chromatography. The N-terminal Trx tag or GST tag was cleaved by HRV 3C protease, and then further removed by HisTrap excel column (GE Healthcare, 17371205) or GSTrap HP column (GE Healthcare, 17528202), respectively. For proteins used in crystal screening, the GST-tagged RNF213 RING and N-terminal methionine extended IpaH1.4 LRR (residues 38-271) were co-expressed in Rosetta (DE3) *E. coli* cells.

For protein expression of the full length RNF213 or N-terminal truncated RNF213 fragment in HEK293F cells. HEK293F cells (ATCC) lacking *N*-acetylglucosaminyltransferase I (Gnt1) were grown in Union-293 Medium (Union-Biotech, UPI000) in a shaker incubator set at 37 °C, 110 rpm, 30% humidity, and 5% CO₂. The indicated plasmids were transfected to HEK293F cells for 4 days using PEI 40 K (Polysciences, 24765-100). The transfected cells were collected and lysed in the lysis buffer containing 50 mM HEPES, 200 mM KCl, 1 mM DTT, 1 mM PMSF, 1 μg/mL Aprotinin, 1 μg/mL Pepstatin, and 1 μg/mL Leupeptin at pH 7.3. The lysate was centrifuged at $37,000 \times g$ for 40 min at 4 °C. The supernatant was collected and incubated with anti-FLAG beads (GenScript, L00432) for 2 h at 4 °C. The beads were washed four times with the cold buffer containing 50 mM HEPES, 200 mM KCl and 1 mM DTT at pH 7.3, and then incubated with HRV 3C protease overnight at 4 °C to remove the 3×FLAG-6×His tag. The flow-through and 4 mL of wash were collected and concentrated using Amicon Ultra 15 ml 100 kDa cut-off centrifugal filters (Millipore, UFC5100). Concentrated proteins were loaded onto a Superose 6 increase 10/300 GL column (GE Healthcare, 29091596) for further purification.

GST pull-down assay

Direct interaction of the wild type IpaH1.4 with relevant FLAG-tagged proteins were analyzed in the assay buffer containing 20 mM Tris, 100 mM NaCl, 1 mM DTT, 0.5% NP-40, and 1% Glycerol, at pH 7.5. 100 μg GST-tagged IpaH1.4 or GST tag were pelleted by adding 20 μL of fresh glutathione sepharose 4B beads (GE Healthcare, 17075601). The pellets were washed three times with 1 mL of the assay buffer, and subsequently added 2 mL cell lysis containing overexpressed relevant FLAG-tagged protein, which incubated on ice for another 1.5 h. Then, the pellets were washed four times with 1 mL of the assay buffer. Finally, the pellets were boiled with 30 μL of the SDS-PAGE sample buffer. The samples were detected by western blot using specific GST antibody (1:2000 dilution; Proteintech, 10000-0-AP) and FLAG antibody (1:2000 dilution; Proteintech, 20543-1-AP)

Analytical ultracentrifugation

Sedimentation velocity experiments in this study were performed on a Beckman ProteomeLab XL-I analytical ultracentrifuge equipped with an eight-cell rotor under 40,000 rpm at 20 °C. The partial specific volumes of different protein samples and the relevant buffer densities were calculated using the software SEDNTERP (<http://www.rasmb.org/>). The final sedimentation velocity data were analyzed and fitted to a continuous sedimentation coefficient distribution model using the program SEDFIT³⁹. The fitting results were further output to the Origin 9 software and aligned with each other.

Size exclusion chromatography

All size exclusion chromatography (SEC) analyses were performed using an AKTA FPLC system (GE Healthcare) with absorbance monitored at 280 nm. Individual protein samples (1 mg/mL) and mixed protein samples (each protein at a final concentration of 1 mg/mL) were prepared in a volume of 500 μL. Prior to loading, mixed protein samples were incubated at 4 °C for 2 h. The samples were then loaded onto either a Superose 6 Increase 10/300 GL column (GE Healthcare, 29091596) or a Superdex 75 10/300 GL column (GE Healthcare, 17517401), both pre-equilibrated with the same column buffer using in protein purification. The resulting chromatographic data were analyzed and fitted using Origin 9 software, with the outputs aligned for comparative analysis.

Multi-angle light scattering analysis

For multi-angle light-scattering (MALS) measurement, RNF213(371-5207) sample was injected into an AKTA FPLC system (GE Healthcare) with a Superose 6 increase 10/300 GL column with the buffer containing 50 mM HEPES (pH 7.3), 200 mM KCl and 1 mM DTT. The chromatography system was coupled to a static light scattering detector (miniDawn, Wyatt Technology) and a differential refractive index detector (Optilab, Wyatt Technology). Data were collected every 0.5 s with a flow rate of 0.5 mL/min. Data were analyzed using the ASTRA 6 software (Wyatt Technology) and drawn on the Origin 9 software.

Isothermal titration calorimetry (ITC) assay

ITC experiments were performed using an automated ITC calorimeter (Malvern) at 25 °C. All protein samples used in ITC experiments were prepared in the same buffer containing 20 mM Tris-HCl (pH 7.5), 100 mM NaCl and 1 mM DTT. The titration data were analyzed using the Malvern MicroCal PEAQ-ITC analysis program and fitted using the one-site binding mode. The output results were further drawn using the Origin 9 software.

In vitro ubiquitination assay

Recombinant murine UBA1 (E1), relevant human E2s and ubiquitin proteins (wild type ubiquitin or ubiquitin variants) expressed in *E. coli* cells were used for the assay. The Cy5-labeled ubiquitin was generated by labeling the purified 6×His-Cys-ubiquitin with Cy5-Maleimide Mono-Reactive Dye (Cytiva, PA15131). A typical reaction system used for the in vitro ubiquitination assays containing 1 μM UBA1, 4 μM E2, 4 μM IpaH1.4, 25 μM ubiquitin and 0.2 μM RNF213 in a buffer with 20 mM Tris-HCl, 100 mM NaCl, 1 mM DTT, 10 mM ATP and 10 mM MgCl₂ at pH 7.5. Reaction mixtures were incubated at 37 °C for the desired time, and aliquots of samples were immediately denatured by mixing with 2×SDS-PAGE sample buffer with 100 mM DTT and boiled for 10 min at 65 °C. For in vitro ubiquitination assay using fluorescent Cy5-labeled ubiquitin, 5 μM Cy5-labeled ubiquitin was used to replace equivalent un-labeled ubiquitin. Finally, samples were analyzed by SDS-PAGE followed by fluorescence imaging or Coomassie blue staining.

Affinity purification and sample preparation for MS analysis

For each plasmid, three replicate HEK293F cell samples were prepared. The transfection complex was formed by mixing 25 μg of plasmid with 62.5 μL of PEI 40 K (Polysciences, 24765-100), followed by a 15-min incubation at room temperature. The transfection mixture was then added to a 25 mL cell culture flask containing HEK293F cells at a density of 2,000,000 cells per milliliter. After transfection, the medium was not replaced, and the cells were cultured for an additional 3 days under standard conditions. The cells were collected and lysed in the lysis buffer containing 20 mM Tris, 200 mM NaCl, 2 mM MgCl₂, 1 mM DTT, 1% Triton X-100, 500 μM PMSF, 1 μg/mL Aprotinin, 1 μg/mL Pepstatin,

and 1 µg/mL Leupeptin at pH 7.5. The lysate was centrifuged at 16,000 × *g* for 20 min at 4 °C. The supernatant was collected and incubated with anti-FLAG beads (GenScript, L00432) for 2 h at 4 °C. The beads were washed four times with a cold buffer containing 20 mM Tris, 150 mM NaCl, 1 mM DTT, 5% glycerol at pH 7.5, and then incubated with TEV protease overnight at 4 °C to remove the 3×FLAG tag. The supernatant was used for the further mass spectrometric analysis.

Six volumes of pre-chilled acetone were added to the sample to precipitate the proteins overnight at −20 °C. The protein pellet was dried by using a Speedvac for 1–2 min. The pellet was subsequently dissolved in 8 M urea, 100 mM Tris-HCl, pH 8.5. TCEP (the final concentration is 5 mM) and iodoacetamide (the final concentration is 10 mM) (Sigma, I1149-25G) for reduction and alkylation were added to the solution and incubated at room temperature for 30 min, respectively. The protein mixture was diluted four times and digested overnight with Trypsin at 1:50 (w/w). The tryptic-digested peptide solution was desalted using a MonoSpin™ C18 column and dried with a SpeedVac.

In-gel digestion for MS analysis

The Coomassie Brilliant Blue stained gel band was excised into small pieces and washed in order with water, 50 mM NH₄HCO₃ in 50% acetonitrile and 100% acetonitrile. The protein was reduced with 10 mM TCEP (Thermo Fisher Scientific, 20491) in 100 mM NH₄HCO₃ at room temperature for 30 min and alkylated with 55 mM N-ethylmaleimide (Thermo Fisher Scientific, 23030) in 100 mM NH₄HCO₃ in the dark for 30 min. After that, the gel pieces were washed with 100 mM NH₄HCO₃ and 100% acetonitrile, and then dried using a SpeedVac. Finally, they were digested with 12.5 ng/µL trypsin (Promega, <http://www.promega.com/>, V5280) in 50 mM NH₄HCO₃ for 16 h at 37 °C, and the tryptic peptides were extracted twice with 50% acetonitrile/5% formic acid and dried using a SpeedVac. The sample was reconstituted with 0.1% formic acid, desalted using a MonoSpin™ C18 column (5010-21701, GL Science), and then dried with a SpeedVac.

LC-MS/MS and data analysis

The peptide mixture was analyzed by a home-made 30 cm-long pulled-tip analytical column (75 µm ID packed with ReproSil-Pur C18-AQ 1.9 µm resin, Dr. Maisch GmbH, Germany), the column was then placed in-line with an Easy-nLC 1200 nano HPLC (Thermo Fisher Scientific) for mass spectrometry analysis. The analytical column temperature was set at 55 °C during the experiments. The mobile phase and elution gradient used for peptide separation were as follows: 0.1% formic acid in water as buffer A and 0.1% formic acid in 80% acetonitrile as buffer B, 0–1 min, 2%–10% B; 1–81 min, 10–35% B; 81–96 min, 35%–60% B, 96–111 min, 60%–100% B, 111–120 min, 100% B. The flow rate was set as 300 nL/min.

Data-dependent MS/MS analysis was performed with a Q Exactive Orbitrap mass spectrometer (Thermo Fisher Scientific). Peptides eluted from the LC column were directly electrosprayed into the mass spectrometer with the application of a distal 2.2-kV spray voltage. A cycle of one full-scan MS spectrum (*m/z* 300–1800) was acquired followed by top 20 MS/MS events, sequentially generated on the first to the twentieth most intense ions selected from the full MS spectrum at a 30% normalized collision energy. Full scan resolution was set to 70,000 with automated gain control (AGC) target of 3e6. MS/MS scan resolution was set to 17,500 with isolation window of 1.8 *m/z* and AGC target of 1e5. The number of microscans was one for both MS and MS/MS scans and the maximum ion injection time was 50 and 100 ms, respectively. The setting for precursor ion selection was as follows: charge exclusion, 1 and >8; exclude isotopes, on; and exclusion duration, 30 s. MS scan functions and LC solvent gradients were controlled by the Xcalibur data system (Thermo Fisher Scientific).

For analysis of IpaH1.4-binding proteins in HEK293F cells, all the acquired raw data were analyzed together by MaxQuant V2.1.4.0

against a UniProtKB Homo Sapiens database using the default settings. Meanwhile, the “match between runs” was performed. Tolerance of precursor mass and fragment mass were set to ±20 ppm. The main search peptides tolerance was setting at 4.5 ppm according to the feature of the instrument in the study. Oxidation (M) and acetylation (protein N term) were specified as variable modifications, and carbamidomethyl (C) was specified as fixed modification. Trypsin was defined as cleavage enzyme, and the maximum missing cleavage was set at 2. All identified proteins had an FDR of 1%. Replicate samples were grouped, proteins with less than three valid values in at least one group were removed and missing values were imputed with the minimal value of the group to compile a list of quantified proteins. A total of 611 proteins were quantified in the IpaH1.4 C368A group and 572 proteins were quantified in the IpaH1.4 LRR group. On the quantified proteins, a two-tailed unpaired Student's *t* test analysis was performed with the control condition to reveal specific binding proteins for each IpaH1.4 bait. The results of these *t*-tests are shown in the volcano plot. For each protein, the log₂ (IpaH1.4/control) fold change value is indicated on the *X*-axis, while the statistical significance (−log₁₀ *p* value) is indicated on the *Y*-axis (Supplementary Data 1). Proteins outside the curved lines, set by fold change value of 32 and *p* value of 0.05, represent specific IpaH1.4-binding proteins.

For analysis of ubiquitin modification sites on RNF213(371-5207), the acquired MS/MS data were analyzed against a Swiss-Prot *Homo Sapiens* database using PEAKS Studio X+ (Bioinformatics Solutions). The database search parameters were set as the followings: MS and MS/MS tolerance of 20 ppm and 0.1 Da, respectively, FDR was set as 1% and protein identification threshold was set as (−10 log₁₀ *p*) ≥ 20. Oxidation (M) and ubiquitin (K) were specified as variable modifications, and N-ethylmaleimide (C) was specified as fixed modification. For residues with high conservation and an Ascore value > 20, they were selected as ubiquitination sites with high confidence (Supplementary Data 2).

EM sample preparation and data collection

Initial validation of sample homogeneity was conducted through negative staining with 0.2% (w/v) uranyl acetate using a Tecnai T12 Transmission Electron Microscope (Thermo Fisher Scientific). Subsequently, for cryo-EM analysis, the sample was adjusted to 0.4 mg/mL and aliquots of 4 microliters were applied to glow-discharged 200 mesh 2/1 Au grids (Quantifoil, NI-C15nAu20-01). Following a 5-s incubation period, grids were blotted for 2 s with a blot force of −2 within a VitroBot Mark IV chamber (Thermo Fisher Scientific) set at 4 °C and 100% humidity, then rapidly plunged into pre-cooled liquid ethane.

Cryo-EM data acquisition was performed using a 300 kV Titan Krios G4 microscope (Thermo Fisher Scientific) equipped with a Biocontinuum K3 Direct Electron Detector and a GIF filter (Gatan). Movies were recorded at a nominal magnification of ×81,000, corresponding to a calibrated pixel size of 0.5275 Å per pixel in super-resolution mode, with defocus ranging from −1.2 to −2.4 µm. Beam image-shift was used to accelerate the data collection in EPU software package. Exposures of 2.2 s were dose-fractionated into 40 frames (55 ms per frame) with a dose rate of 25 e[−] per pixel/s (roughly 1.235 e[−]/Å² per frame), resulting in a total dose of 49.41 e[−]/Å².

Image processing

The collected movie stacks were gain-normalized, binned, dose-weighted, and motion-corrected in Motioncor2⁶⁰. The CTF parameters were determined with CTFFIND4⁶¹. Particles were automatically picked using Gautomatch (<https://www2.mrc-lmb.cam.ac.uk/download/gautomatch-053/>). Subsequently, particles were extracted and subjected to 2D classification in RELION-3.1⁶². Those particles showing secondary structure features in the 2D classes were selected and subjected to CryoSPARC⁶³ heterogeneous refinement using the map EMD-10429⁵⁰ as initial reference (the cryoSPARC ab initio

reconstruction was also tested, but the maps from heterogeneous refinement exhibited better quality). The 3D classes showing clear structural features were selected and refined using CryoSPARC non-uniform refinement. To improve the map quality of the density of IpaH1.4, the density in the cyan mask (Supplementary Fig. 8b) was subjected to CryoSPARC local refinement and then subtracted. The remained density (RNF213 E3 module and IpaH1.4) was first subjected to local refinement with the purple mask (Supplementary Fig. 8b). Then particles were subjected to focus 3D classification with a purple solvent mask and an orange focus mask (Supplementary Fig. 8b). The particles in the 3D classes with clearer IpaH1.4 density were combined and used for local refinement.

Model building

The local installed AlphaFold2⁶⁴ predicted structures of human RNF213 (UniProt Proteomes identifier: [UP000005640](#); UniProt accession [Q63HN8-3](#)) and *S. flexneri* IpaH1.4 (UniProt Proteomes identifier: [UP000001006](#); UniProt accession [AOA0H2USG1](#)) served as initial models. These models were initially fitted into cryo-EM density maps using UCSF Chimera⁶⁵, and subsequently refined through manual adjustments in Coot⁶⁶. Iterative cycles of the `real_space_refine` in PHENIX⁶⁷, and further manual adjustments in Coot were employed to optimize the models. Detailed statistical data regarding the model building process can be found in Supplementary Table 1.

Protein crystallization and structural elucidation

Crystals of the RNF213 RING/IpaH1.4 LRR complex were obtained using the hanging-drop vapor-diffusion method at 16 °C. The crystal-growing condition of the RNF213 RING/IpaH1.4 LRR complex (20.0 mg/mL) was 0.1 M HEPES (pH 7.8), 0.2 M Ammonium acetate and 20% (w/v) polyethylene glycol 3350. A 1.7 Å resolution X-ray data set for the RNF213 RING/IpaH1.4 LRR complex was collected at the beamline BLO2UI of the Shanghai Synchrotron Radiation Facility⁶⁸. The diffraction data were processed and scaled using autoPROC⁶⁹.

The phase problem of the RNF213 RING/IpaH1.4 LRR complex was solved by molecular replacement method using the IpaH1.4 LRR structure (PDB ID: 7V8H [<https://doi.org/10.2210/pdb7V8H/pdb>]) as the search model with PHASER⁷⁰. The initial structural models were rebuilt manually using COOT⁶⁶, and then refined using PHENIX⁶⁷. Further manual model building and adjustments were completed using COOT⁶⁶. The qualities of the final models were validated by MolProbity⁷¹. The final refinement statistics of solved structure in this study were listed in Supplementary Table 2. All the structural diagrams were prepared using the program PyMOL (<http://www.pymol.org/>) or UCSF ChimeraX⁷².

Cell culture and co-immunoprecipitation assays

The HEK293T (ATCC, CRL-1573) and HeLa (ATCC, CCL-2) cell lines were kindly provided by Prof. Junying Yuan from Interdisciplinary Research Center on Biology and Chemistry, CAS, China. All cells were cultured in Dulbecco's modified Eagle's medium (DMEM; Thermo Fisher Scientific, 11965092) supplemented with 10% fetal bovine serum (Sigma, F8318) and 1% penicillin-streptomycin (Thermo Fisher Scientific, 15140122) at 37 °C in humidified 5% CO₂ atmosphere. All cell lines were tested negative for *Mycoplasma* by using standard PCR method. Co-transfections of AcGFP-RNF213 and FLAG-mCherry-IpaH1.4 or related mutant plasmids were performed with Lipofectamine 2000 (Thermo Fisher Scientific, 11668019) according to the manufacturer's instructions. After 24 h, the HEK293T cells transiently expressing proteins were harvested, washed with the PBS buffer, and lysed at 4 °C in a lysis buffer containing 50 mM HEPES (pH 7.3), 200 mM KCl, 1 mM DTT, 500 μM PMSF, 1 μg/mL Aprotinin, 1 μg/mL Pepstatin, and 1 μg/mL Leupeptin. Lysates were centrifuged at 16,000 × *g* for 20 min at 4 °C, and then the supernatants were incubated with anti-GFP monoclonal antibody-agarose (MBL, D153-8) for 30 min at 4 °C. Precipitated

proteins were washed with the cold lysis buffer for 5 times, and collected by centrifugation at 3000 × *g* for 3 min at 4 °C. Then, the beads were resuspended with 2×SDS-PAGE sample buffer containing 100 mM DTT and boiled for 10 min at 65 °C. Subsequently, the precipitated proteins were resolved in SDS-PAGE gel and the GFP-tagged RNF213 and FLAG-mCherry-tagged IpaH1.4 were detected by western blot using specific GFP antibody (1:2000 dilution; Proteintech 50430-2-AP) and mCherry antibody (1:4000 dilution; abcam, ab183628), respectively.

Immunoblot analysis

Post-nuclear supernatants from HeLa cells were lysed in a lysis buffer containing 50 mM HEPES pH 7.3, 200 mM KCl, 1 mM DTT, 500 μM PMSF, 1 μg/mL Aprotinin, 1 μg/mL Pepstatin, and 1 μg/mL Leupeptin. Cleared supernatants were mixed with 2×SDS-PAGE sample buffer with 100 mM DTT and boiled for 10 min at 65 °C. An overnight wet transfer was used to transfer RNF213 proteins onto methanol-activated PVDF membranes (Millipore, ISEQ00010). The samples were detected by western blot using specific GFP antibody (1:2000 dilution; Proteintech, 50430-2-AP), mCherry antibody (1:4000 dilution; abcam, ab183628), and GAPDH antibody (1:400,000; Sangon, D110016), respectively. Additionally, RNF213 protein was specifically detected by using the RNF213 antibody (1:500 dilution; Sigma, HPA003347) in Fig. 2f and the RNF213 antibody (1:1000 dilution; MILLIPORE, ABN1474) in Fig. 2g.

Immunofluorescence microscopy

After infected by *S. flexneri* 4 h, AcGFP-RNF213 stable HeLa cells were fixed with 4% paraformaldehyde for 15 min and punched with 0.2% Triton X-100 in PBS for another 15 min at room temperature, and the nuclei were visualized by staining with 4', 6-diamidino-2-phenylindole (DAPI). The cell images were captured and analyzed using the TCS SP5 confocal microscope equipped with LAS X software (Leica). In particular, ubiquitinated substrates were stained by incubating UBCJ2 antibody (1:100; Enzo, ENZ-ABS840) overnight at 4 °C and goat anti-mouse Alexa Fluor 555 (1:500; Thermo Fisher Scientific, A-21422) for 40 min at room temperature. The statistical data represent means ± SEM of >30 analyzed cells (selected regions). Statistical analyses were performed in GraphPad Prism 6.01.

Generation of RNF213-knockout cells

The *RNF213* gene was knocked out in HeLa cells using the CRISPR-Cas9 system. Oligonucleotides for the single guide RNA (sgRNA) (sequence: CAGTTGGCAAGAAAACCCCG) were phosphorylated with T4 PNK (New England Biolabs) and cloned into the LentiCRISPR v2 vector and co-transfected into HEK293T cells with pMD2.G and psPAX2 vectors using Lipofectamine 2000 transfection reagent (Thermo Fisher Scientific, 11668019). In order to increase the virus titer, the virus-containing medium was filtered using a 0.45 μm-pore syringe filter, and concentrated by using Lentiviral concentration reagent (Biodragon, BF06205). HeLa cells were then incubated with polybrene (Sigma, TR-1003) and virus-containing medium. Transfected HeLa cells were treated with puromycin (1.0 μg/ml; InvivoGen, ant-pr-5), and single cells were sorted into a 96-well plate. Expanded single colonies were screened for the lack of RNF213 expression by immunoblotting, and further confirmed by DNA sequencing.

Generation of AcGFP-RNF213 stable cell lines

An modified passer transposon system was used in this work to generate AcGFP-RNF213 stable cell lines⁷³. The AcGFP-tagged RNF213 was cloned into the pJL-NeoR vector and was co-transfected into RNF213-knockout cells with pJL-SB vector using Lipofectamine 2000 transfection reagent (Thermo Fisher Scientific, 11668019). Notably, the sgRNA-targeting region of *RNF213* at pJL-NeoR vector was synonymously mutated to avoid being targeted again by Cas9 enzyme. After 2 days, cells were treated with G418 (600.0 μg/mL; Beyotime, ST081), and further confirmed by DNA sequencing.

Bacterial strain generation and infection

S. flexneri 2a strain M90T was used in this work. Double knockout of the *ipaH1.4/ipaH2.5* gene was constructed by λ red recombinase-mediated replacement by homologous recombination with a kanamycin resistance cassette, followed by flippase recombinase-catalyzed removal of the cassette. To rescue the *ipaH1.4/ipaH2.5*-knockout strain, the wild-type or mutant *ipaH1.4* gene, which has a C-terminal 6×His tag gene sequence, was introduced back into the *ipaH1.4* locus on the chromosome in the knockout strain by a CRISPR-Cas12a-assisted recombination method. Successful rescues of different *ipaH1.4* genes were verified by DNA sequencing.

To enumerate intracellular bacteria, HeLa cells were seeded in 24-well plates 24 h before infection. Bacteria were diluted in DMEM to achieve the desired multiplicity of infection (MOI) of 100. Infection was accelerated by centrifugation at 500 × g for 10 min at room temperature followed by incubation at 37 °C in a 5% CO₂ incubator. After 1 h of infection, the infected cells were washed three times with PBS. To kill extracellular bacteria, the medium was then replaced with DMEM supplemented with 50 µg/mL gentamycin and incubated for an additional 1 h or 5 h. To determine intracellular *S. flexneri* colony-forming units (CFUs), cells were lysed in 1 mL of the PBS buffer containing 0.1% Triton X-100. Serial dilutions were plated in duplicate on LB agar and grown overnight. The data are presented as means ± SEM from three independent experiments. Statistical analyses were performed in GraphPad Prism 6.01.

For immunoblot analyses of endogenous RNF213 degradation, HeLa cells were seeded in 60 mm dishes 24 h before infection. Bacteria was resuspended in DMEM without dilution, 1 mL of the bacterial suspension were added per dish. Infection was performed by incubation at 37 °C in a 5% CO₂ incubator. After 4 h of infection, the infected cells were washed three times with PBS. To kill extracellular bacteria, the medium was then replaced with DMEM supplemented with 50 µg/mL gentamycin and incubated for an additional 20 h.

For fluorescence imaging, AcGFP-RNF213 stable HeLa cells or AcGFP-RNF213 L4036R stable HeLa cells were seeded in 15 mm glass bottom cell culture dishes (NEST, 801002) 48 h before infection. Transfections of FLAG-mCherry or FLAG-mCherry-IpaH1.4 related mutant plasmids were performed with Lipofectamine 2000 (Thermo Fisher Scientific, 11668019) 24 h before infection. Bacteria was resuspended in DMEM without dilution, 0.2 mL of the bacterial suspension were added per dish. Infection was performed by incubation at 37 °C in a 5% CO₂ incubator. After 4 h of infection, the infected cells were washed three times with PBS and fixed with 4% paraformaldehyde for 15 min for further microscopy experiment.

RNA isolation and quantitative RT-PCR

Total cellular RNA was extracted using RNA Isolation Kit (Vazyme). The cDNA was synthesized using the HiScript III RT SuperMix kit (Vazyme). The following primers were used for quantitative RT-PCR: RNF213 (forward) (GGAAAGGAAACCTCTGAACTCGG); RNF213 (reverse) (CTCGTTCTGGTCTCTGAGCATG). The GAPDH gene was used as an internal control for quantitative gene expression analyses.

Reporting summary

Further information on research design is available in the Nature Portfolio Reporting Summary linked to this article.

Data availability

The raw proteomics data have been deposited to the ProteomeXchange Consortium (<https://proteomecentral.proteomexchange.org>) with the dataset identifier [PXD060669](https://proteomecentral.proteomexchange.org/dataset/PXD060669) via the iProX partner repository^{74,75}. The cryo-EM density maps and structural models generated in this study have been deposited in the Electron Microscopy Data Bank (EMDB) and the Protein Data Bank (PDB) under the following accession numbers: [EMD-61848](https://www.ebi.ac.uk/emdb/EMD-61848) (RNF213), [EMD-61852](https://www.ebi.ac.uk/emdb/EMD-61852) (RNF213_E3_module-IpaH1.4_LRR_domain), and [EMD-9JWG](https://www.ebi.ac.uk/emdb/EMD-9JWG) (RNF213_E3_module-IpaH1.4_LRR_domain). The atomic coordinate and structure factors of the crystal structure of the RNF213 RING/IpaH1.4 LRR complex have been deposited in the PDB under the accession code [9JTA](https://www.rcsb.org/entry/9JTA). PDB codes of previously published structures used in this study are [5AIT](https://www.rcsb.org/entry/5AIT) and [7V8H](https://www.rcsb.org/entry/7V8H). Source data are provided with this paper.

[9JWG](https://www.rcsb.org/entry/9JWG) (RNF213_E3_module-IpaH1.4_LRR_domain) and [9JWG](https://www.rcsb.org/entry/9JWG) (RNF213_E3_module-IpaH1.4_LRR_domain). The atomic coordinate and structure factors of the crystal structure of the RNF213 RING/IpaH1.4 LRR complex have been deposited in the PDB under the accession code [9JTA](https://www.rcsb.org/entry/9JTA). PDB codes of previously published structures used in this study are [5AIT](https://www.rcsb.org/entry/5AIT) and [7V8H](https://www.rcsb.org/entry/7V8H). Source data are provided with this paper.

References

- Ciechanover, A. The unravelling of the ubiquitin system. *Nat. Rev. Mol. Cell Biol.* **16**, 322–324 (2015).
- Pickart, C. M. & Eddins, M. J. Ubiquitin: structures, functions, mechanisms. *Biochim. Biophys. Acta* **1695**, 55–72 (2004).
- Weissman, A. M. Themes and variations on ubiquitylation. *Nat. Rev. Mol. Cell Biol.* **2**, 169–178 (2001).
- Komander, D. & Rape, M. The ubiquitin code. *Annu. Rev. Biochem.* **81**, 203–229 (2012).
- Otten, E. G. et al. Ubiquitylation of lipopolysaccharide by RNF213 during bacterial infection. *Nature* **594**, 111–116 (2021).
- Kelsall, I. R. et al. HOIL-1 ubiquitin ligase activity targets unbranched glucosaccharides and is required to prevent polyglucosan accumulation. *EMBO J.* **41**, e109700 (2022).
- Yang, C. S. et al. Ubiquitin modification by the E3 ligase/ADP-ribosyltransferase Dtx3L/Parp9. *Mol. Cell* **66**, 503–516.e505 (2017).
- Popovic, D., Vucic, D. & Dikic, I. Ubiquitination in disease pathogenesis and treatment. *Nat. Med.* **20**, 1242–1253 (2014).
- Mukherjee, R. & Dikic, I. Regulation of host-pathogen interactions via the ubiquitin system. *Annu. Rev. Microbiol.* **76**, 211–233 (2022).
- Shaid, S., Brandts, C. H., Serve, H. & Dikic, I. Ubiquitination and selective autophagy. *Cell Death Differ.* **20**, 21–30 (2013).
- Vargas, J. N. S., Hamasaki, M., Kawabata, T., Youle, R. J. & Yoshimori, T. The mechanisms and roles of selective autophagy in mammals. *Nat. Rev. Mol. Cell Biol.* **24**, 167–185 (2023).
- Wild, P. et al. Phosphorylation of the autophagy receptor optineurin restricts Salmonella growth. *Science* **333**, 228–233 (2011).
- Zheng, Y. T. et al. The adaptor protein p62/SQSTM1 targets invading bacteria to the autophagy pathway. *J. Immunol.* **183**, 5909–5916 (2009).
- Li, F. X. et al. Structural insights into the ubiquitin recognition by OPTN (optineurin) and its regulation by TBK1-mediated phosphorylation. *Autophagy* **14**, 66–79 (2018).
- Thurston, T. L., Ryzhakov, G., Bloor, S., von Muhlen, N. & Randow, F. The TBK1 adaptor and autophagy receptor NDP52 restricts the proliferation of ubiquitin-coated bacteria. *Nat. Immunol.* **10**, 1215–1221 (2009).
- Xie, X. Q. et al. Molecular basis of ubiquitin recognition by the autophagy receptor CALCOCO2. *Autophagy* **11**, 1775–1789 (2015).
- Rogov, V., Dotsch, V., Johansen, T. & Kirkin, V. Interactions between autophagy receptors and ubiquitin-like proteins form the molecular basis for selective autophagy. *Mol. Cell* **53**, 167–178 (2014).
- Gomes, L. C. & Dikic, I. Autophagy in antimicrobial immunity. *Mol. Cell* **54**, 224–233 (2014).
- Levine, B., Mizushima, N. & Virgin, H. W. Autophagy in immunity and inflammation. *Nature* **469**, 323–335 (2011).
- Yamamoto, H., Zhang, S. D. & Mizushima, N. Autophagy genes in biology and disease. *Nat. Rev. Genet.* **24**, 382–400 (2023).
- Liu, S. & Chen, Z. J. Expanding role of ubiquitination in NF- κ B signaling. *Cell Res.* **21**, 6–21 (2011).
- Iwai, K., Fujita, H. & Sasaki, Y. Linear ubiquitin chains: NF- κ B signalling, cell death and beyond. *Nat. Rev. Mol. Cell Biol.* **15**, 503–508 (2014).
- van Wijk, S. J. L. et al. Linear ubiquitination of cytosolic Salmonella Typhimurium activates NF- κ B and restricts bacterial proliferation. *Nat. Microbiol.* **2**, 17066 (2017).

24. Randow, F. & Youle, R. J. Self and nonself: how autophagy targets mitochondria and bacteria. *Cell Host Microbe* **15**, 404–412 (2014).
25. Pollaci, G. et al. Novel multifaceted roles for RNF213 protein. *Int. J. Mol. Sci.* **23**, <https://doi.org/10.3390/ijms23094492> (2022).
26. Morito, D. Molecular structure and function of mysterin/RNF213. *J. Biochem.* **175**, 495–505 (2024).
27. Kamada, F. et al. A genome-wide association study identifies as the first Moyamoya disease gene. *J. Hum. Genet.* **56**, 34–40 (2011).
28. Liu, W. Y. et al. Identification of as a susceptibility gene for moyamoya disease and its possible role in vascular development. *PLoS ONE* **6**, e22542 (2011).
29. Kobayashi, H. et al. Biochemical and functional characterization of RNF213 (Mysterin) R4810K, a susceptibility mutation of moyamoya disease, in angiogenesis in vitro and in vivo. *J. Am. Heart Assoc.* **4**, <https://doi.org/10.1161/JAHA.115.002146> (2015).
30. Sugihara, M. et al. The AAA+ ATPase/ubiquitin ligase mysterin stabilizes cytoplasmic lipid droplets. *J. Cell Biol.* **218**, 949–960 (2019).
31. Pol, A., Gross, S. P. & Parton, R. G. Review: biogenesis of the multifunctional lipid droplet: lipids, proteins, and sites. *J. Cell Biol.* **204**, 635–646 (2014).
32. Bosch, M. et al. Mammalian lipid droplets are innate immune hubs integrating cell metabolism and host defense. *Science* **370**, eaay8085 (2020).
33. Houzelstein, D. et al. The ring finger protein 213 gene (Rnf213) contributes to Rift Valley fever resistance in mice. *Mamm. Genome* **32**, 30–37 (2021).
34. They, F. et al. Ring finger protein 213 assembles into a sensor for ISGylated proteins with antimicrobial activity. *Nat. Commun.* **12**, 5772 (2021).
35. Tian, H. et al. RNF213 modulates gamma-herpesvirus infection and reactivation via targeting the viral replication and transcription activator. *Proc. Natl Acad. Sci. USA* **120**, e2218825120 (2023).
36. Hernandez, D., Walsh, S., Saavedra Sanchez, L., Dickinson, M. S. & Coers, J. Interferon-inducible E3 ligase RNF213 facilitates host-protective linear and K63-linked ubiquitylation of toxoplasma gondii parasitophorous vacuoles. *mBio* **13**, e0188822 (2022).
37. Walsh, S. C. et al. The bacterial effector GarD shields Chlamydia trachomatis inclusions from RNF213-mediated ubiquitylation and destruction. *Cell Host Microbe* **30**, 1671–1684.e1679 (2022).
38. Jennison, A. V. & Verma, N. K. Shigella flexneri infection: pathogenesis and vaccine development. *FEMS Microbiol. Rev.* **28**, 43–58 (2004).
39. Khalil, I. A. et al. Morbidity and mortality due to shigella and enterotoxigenic diarrhoea: the Global Burden of Disease Study 1990–2016. *Lancet Infect. Dis.* **18**, 1229–1240 (2018).
40. Tanner, K., Brzovic, P. & Rohde, J. R. The bacterial pathogen-ubiquitin interface: lessons learned from Shigella. *Cell. Microbiol.* **17**, 35–44 (2015).
41. Xian, W. et al. The Shigella kinase effector OspG modulates host ubiquitin signaling to escape septin-cage entrapment. *Nat. Commun.* **15**, 3890 (2024).
42. Ashida, H. et al. A bacterial E3 ubiquitin ligase IpaH9.8 targets NEMO/IKKgamma to dampen the host NF-kappaB-mediated inflammatory response. *Nat. Cell Biol.* **12**, 66–73 (2010).
43. Sanada, T. et al. The Shigella flexneri effector OspI deamidates UBC13 to dampen the inflammatory response. *Nature* **483**, 623–626 (2012).
44. de Jong, M. F., Liu, Z., Chen, D. & Alto, N. M. Shigella flexneri suppresses NF-kappaB activation by inhibiting linear ubiquitin chain ligation. *Nat. Microbiol.* **1**, 16084 (2016).
45. Pruneda, J. N. et al. The molecular basis for ubiquitin and ubiquitin-like specificities in bacterial effector proteases. *Mol. Cell* **63**, 261–276 (2016).
46. Ashida, H. & Sasakawa, C. IpaH family effectors as a versatile model for studying pathogenic bacteria. *Front. Cell Infect. Microbiol.* **5**, 100 (2016).
47. Bullones-Bolanos, A., Bernal-Bayard, J. & Ramos-Morales, F. The NEL family of bacterial E3 ubiquitin ligases. *Int. J. Mol. Sci.* **23**, 7725 (2022).
48. Zhu, Y. et al. Structure of a Shigella effector reveals a new class of ubiquitin ligases. *Nat. Struct. Mol. Biol.* **15**, 1302–1308 (2008).
49. Liu, J. P. et al. Mechanistic insights into the subversion of the linear ubiquitin chain assembly complex by the E3 ligase IpaH1.4 of Shigella flexneri. *Proc. Natl Acad. Sci. USA* **119**, e2116776119 (2022).
50. Ahel, J. et al. Moyamoya disease factor RNF213 is a giant E3 ligase with a dynein-like core and a distinct ubiquitin-transfer mechanism. *Elife* **9**, e56185 (2020).
51. Crespillo-Casado, A. et al. Recognition of phylogenetically diverse pathogens through enzymatically amplified recruitment of RNF213. *EMBO Rep.* **25**, 4979–5005 (2024).
52. Habu, T. & Harada, K. H. UBC13 is an RNF213-associated E2 ubiquitin-conjugating enzyme, and Lysine 63-linked ubiquitination by the RNF213-UBC13 axis is responsible for angiogenic activity. *FASEB Bioadv.* **3**, 243–258 (2021).
53. Takeda, M. et al. Moyamoya disease patient mutations in the RING domain of RNF213 reduce its ubiquitin ligase activity and enhance NFkB activation and apoptosis in an AAA+ domain-dependent manner. *Biochem. Biophys. Res. Commun.* **525**, 668–674 (2020).
54. Hansen, J. M. et al. Pathogenic ubiquitination of GSDMB inhibits NK cell bactericidal functions. *Cell* **184**, 3178–3191.e3118 (2021).
55. Saavedra-Sanchez, L. et al. The Shigella flexneri effector IpaH1.4 facilitates RNF213 degradation and protects cytosolic bacteria against interferon-induced ubiquitylation. *bioRxiv* <https://doi.org/10.1101/2024.09.05.611450> (2024).
56. Naydenova, K. et al. Shigella flexneri evades LPS ubiquitylation through IpaH1.4-mediated degradation of RNF213. *bioRxiv* <https://doi.org/10.1101/2024.09.24.614686> (2024).
57. Branigan, E., Plechanovova, A., Jaffray, E. G., Naismith, J. H. & Hay, R. T. Structural basis for the RING-catalyzed synthesis of K63-linked ubiquitin chains. *Nat. Struct. Mol. Biol.* **22**, 597–602 (2015).
58. Giogha, C. & Pearson, J. S. Shigella shuts down the pyrop-technic show. *Cell Host Microbe* **29**, 1473–1476 (2021).
59. Schuck, P. Size-distribution analysis of macromolecules by sedimentation velocity ultracentrifugation and lamm equation modeling. *Biophys. J.* **78**, 1606–1619 (2000).
60. Zheng, S. Q. et al. MotionCor2: anisotropic correction of beam-induced motion for improved cryo-electron microscopy. *Nat. Methods* **14**, 331–332 (2017).
61. Rohou, A. & Grigorieff, N. CTFIND4: fast and accurate defocus estimation from electron micrographs. *J. Struct. Biol.* **192**, 216–221 (2015).
62. Zivanov, J. et al. New tools for automated high-resolution cryo-EM structure determination in RELION-3. *Elife* **7**, <https://doi.org/10.7554/eLife.42166> (2018).
63. Punjani, A., Rubinstein, J. L., Fleet, D. J. & Brubaker, M. A. cryoSPARC: algorithms for rapid unsupervised cryo-EM structure determination. *Nat. Methods* **14**, 290–296 (2017).
64. Jumper, J. et al. Highly accurate protein structure prediction with AlphaFold. *Nature* **596**, 583–589 (2021).
65. Pettersen, E. F. et al. UCSF Chimera—a visualization system for exploratory research and analysis. *J. Comput. Chem.* **25**, 1605–1612 (2004).
66. Emsley, P. & Cowtan, K. Coot: model-building tools for molecular graphics. *Acta Crystallogr. Sect. D Biol. Crystallogr.* **60**, 2126–2132 (2004).
67. Adams, P. D. et al. PHENIX: building new software for automated crystallographic structure determination. *Acta Crystallogr. Sect. D Biol. Crystallogr.* **58**, 1948–1954 (2002).
68. Wang, Z. et al. Automatic crystal centring procedure at the SSRF macromolecular crystallography beamline. *J. Synchrotron Radiat.* **23**, 1323–1332 (2016).

69. Vonrhein, C. et al. Data processing and analysis with the autoPROC toolbox. *Acta Crystallogr. Sect. D Biol. Crystallogr.* **67**, 293–302 (2011).
70. Storoni, L. C., McCoy, A. J. & Read, R. J. Likelihood-enhanced fast rotation functions. *Acta Crystallogr D.* **60**, 432–438 (2004).
71. Davis, I. W. et al. MolProbity: all-atom contacts and structure validation for proteins and nucleic acids. *Nucleic Acids Res.* **35**, W375–W383 (2007).
72. Meng, E. C. et al. UCSF ChimeraX: tools for structure building and analysis. *Protein Sci.* **32**, e4792 (2023).
73. Wang, S. et al. Passer, a highly active transposon from a fish genome, as a potential new robust genetic manipulation tool. *Nucleic Acids Res.* **51**, 1843–1858 (2023).
74. Ma, J. et al. iProX: an integrated proteome resource. *Nucleic Acids Res.* **47**, D1211–D1217 (2019).
75. Chen, T. et al. iProX in 2021: connecting proteomics data sharing with big data Abstract. *Nucleic Acids Res.* **50**, D1522–D1527 (2022).

Acknowledgements

We thank SSRF BLO2U1, and BL10U2 for X-ray beam time. We thank Yue Yin of the Mass Spectrometry System at the National Facility for Protein Science in Shanghai (NFPS), Shanghai Advanced Research Institute, China for MS data collection and analysis. We thank the Cryo-Electron Microscopy center at the Interdisciplinary Research Center on Biology and Chemistry, Shanghai Institute of Organic Chemistry for help with data collection. This work was supported in part by grants from the Strategic Priority Research Program of the Chinese Academy of Sciences Grant (No. XDB1060000 for L.P.), National Natural Science Foundation of China (32071219, 92253301, 21822705 for L.P., 81830068 for Y.-F.Y., 82472285 for D.W., and 32071297 for J.L.), the National Basic Research Program of China (2022YFC2303102 for L.P.), the CAS Youth Interdisciplinary Team (JCTD-2022-10 for L.P.), the STI2030-Major Projects (2022ZD0207400 for Y.Z.), Shanghai Key Laboratory of Aging Studies (19DZ2260400 for Y.Z.), the Basic Research Pioneer Project by the Science and Technology Commission of Shanghai Municipality (STCSM for Y.Z.), and the Foundation of Key Laboratory of Veterinary Biotechnology, Shanghai, P.R. China (No. BD1500010 for D.W.).

Author contributions

X.Z., H.Z., Y.W., D.W., Y.-F.Y., Yixiao Zhang, and L.P. designed research; X.Z., H.Z., Y.W., D.W., Z.L., Yuchao Zhang, Y.T., J.L. performed research; X.Z., H.Z., Y.W., D.W., Yixiao Zhang, and L.P. analyzed data; X.Z., H.Z., D.W., Y.-F.Y., Yixiao Zhang, and L.P. wrote the paper.

Competing interests

The authors declare no competing interests.

Additional information

Supplementary information The online version contains supplementary material available at <https://doi.org/10.1038/s41467-025-58432-y>.

Correspondence and requests for materials should be addressed to Yu-Feng Yao, Yixiao Zhang or Lifeng Pan.

Peer review information *Nature Communications* thanks Francis Impens, who co-reviewed with Fabien TheryShuya Fukai, and the other, anonymous, reviewers for their contribution to the peer review of this work. A peer review file is available.

Reprints and permissions information is available at <http://www.nature.com/reprints>

Publisher's note Springer Nature remains neutral with regard to jurisdictional claims in published maps and institutional affiliations.

Open Access This article is licensed under a Creative Commons Attribution-NonCommercial-NoDerivatives 4.0 International License, which permits any non-commercial use, sharing, distribution and reproduction in any medium or format, as long as you give appropriate credit to the original author(s) and the source, provide a link to the Creative Commons licence, and indicate if you modified the licensed material. You do not have permission under this licence to share adapted material derived from this article or parts of it. The images or other third party material in this article are included in the article's Creative Commons licence, unless indicated otherwise in a credit line to the material. If material is not included in the article's Creative Commons licence and your intended use is not permitted by statutory regulation or exceeds the permitted use, you will need to obtain permission directly from the copyright holder. To view a copy of this licence, visit <http://creativecommons.org/licenses/by-nc-nd/4.0/>.

© The Author(s) 2025